

Annual Review of Materials Research

Antisymmetry: Fundamentals and Applications

Hari Padmanabhan,^{1,*} Jason M. Munro,^{1,2,*} Ismaila Dabo,^{1,2} and Venkatraman Gopalan^{1,3}

¹Department of Materials Science and Engineering and Materials Research Institute, The Pennsylvania State University, University Park, Pennsylvania 16802, USA; email: hari@psu.edu, jason.munro@gmail.com, dabo@psu.edu, ygopalan@psu.edu

Annu. Rev. Mater. Res. 2020. 50:255-81

First published as a Review in Advance on May 15, 2020

The *Annual Review of Materials Research* is online at matsci.annualreviews.org

https://doi.org/10.1146/annurev-matsci-100219-101404

Copyright © 2020 by Annual Reviews. All rights reserved

*These authors contributed equally to this article

ANNUAL CONNECT

www.annualreviews.org

- Download figures
- Navigate cited references
- · Keyword search
- · Explore related articles
- · Share via email or social media

Keywords

antisymmetry, color symmetry, time reversal, distortion reversal, minimum energy pathways, classification of multivectors

Abstract

Symmetry is fundamental to understanding our physical world. An antisymmetry operation switches between two different states of a trait, such as two time states, position states, charge states, spin states, or chemical species. This review covers the fundamental concepts of antisymmetry and focuses on four antisymmetries, namely, spatial inversion in point groups, time reversal, distortion reversal, and wedge reversion. The distinction between classical and quantum mechanical descriptions of time reversal is presented. Applications of these antisymmetries—in crystallography, diffraction, determining the form of property tensors, classifying distortion pathways in transition state theory, finding minimum energy pathways, diffusion, magnetic structures and properties, ferroelectric and multiferroic switching, classifying physical properties in arbitrary dimensions, and antisymmetry-protected topological phenomena—are described.

²Institutes of Energy and the Environment, The Pennsylvania State University, University Park, Pennsylvania 16802, USA

³Department of Physics and Department of Engineering Science and Mechanics, The Pennsylvania State University, University Park, Pennsylvania 16802, USA

1. INTRODUCTION AND SCOPE

Symmetry is doing something that looks like doing nothing. This statement turns out to be a pretty rigorous basis for the mathematical definition of a symmetry operation. Symmetry lies at the heart of understanding the physical world, from the fundamental laws of physics (1) to materials and their physical properties (2). Any introductory book on materials science (3) begins with a description of crystal structure classified according to crystallographic symmetries. While such symmetry classification dates back to the 1891 work of Fedorov (4) and Schönflies (5; described in 6), the publication in 1913 by Friedrich et al. (7) that crystals are periodic arrays of atoms laid the foundation stone for modern materials science and condensed matter physics.

Antisymmetry is a specific type of symmetry, also called two-color symmetry. The reader is referred to excellent reviews on the topic from decades ago (8, 9). For example, spatial inversion, $\bar{1}$, is an antisymmetry with respect to rotations. Time reversal, 1', is a well-known antisymmetry with applications in magnetic crystallography and in predicting magnetic properties with classical spins. A new antisymmetry, distortion reversal, 1^* , has recently been introduced in predicting minimum energy pathways (MEPs) (10). Another recently formulated antisymmetry, wedge reversion, 1^{\dagger} , enables the classification of physical quantities and properties in arbitrary dimensions (11). This review provides an overview of the fundamental concepts underlying antisymmetry and the specific examples of antisymmetries mentioned above: $\bar{1}$, 1', 1^* , and 1^{\dagger} .

Section 2 introduces the concepts of symmetry, color symmetry, and antisymmetry. Section 3 discusses time-reversal antisymmetry, 1'; its applications to magnetic crystallography and property predictions; and its interpretation in classical versus quantum mechanical contexts. Section 4 discusses distortion-reversal antisymmetry, 1^* , and its applications in finding MEPs. Section 5 introduces a new antisymmetry, wedge reversion, 1^{\dagger} , and its application in classifying multivectors in arbitrary dimensions. Section 6 presents a summary and future outlook, including a brief note on topology. We restrict ourselves to crystallographic symmetry. All the physical problems addressed here are in the nonrelativistic Newtonian framework, where space is considered three-dimensional (3D) and time is considered a scalar quantity disconnected from space. Relativistic space-time involves three fundamental symmetries, of antiparticle conjugation (C), parity (P), and time reversal (T) (13). Parity and time reversal are discussed in the nonrelativistic context as spatial inversion, $\bar{1}$, and time reversal, 1', respectively. Antiparticle conjugation is related to space-time reversal (inverting both space and time coordinates) and is not discussed here further, other than in the nonrelativistic context as $\bar{1}'$.

2. SYMMETRY AND ANTISYMMETRY

2.1. Crystallographic Point and Space Groups; Spatial Inversion, 1; and Neumann's Principle

Rotations are the most common symmetry operations in crystallography. It turns out from simple geometric considerations (see **Figure 1***a*) that periodic crystals can possess only five types of rotational symmetries: 1-, 2-, 3-, 4-, and 6-fold rotations, where a *p*-fold axis refers to rotations of $2\pi/p$ about that axis. This is called the crystallographic restriction theorem and is a direct consequence of the translational periodicity of crystals. If we now consider a periodic crystal, but for the moment ignore translational symmetry, it can be shown that there are only 11 possible ways in which a collection of the above rotational symmetries about different axes can pass through a single point in a self-consistent manner (see **Figure 1***b*). These are the 11 rotational point groups, listed in **Figure 1***c*. The point group 32 is shown as an example in **Figure 1***b*.

Spatial inversion, $\bar{1}$, inverts the space about a single point of inversion, namely, $\bar{1}: r \to -r$. In two dimensions, $\bar{1}$ is equivalent to a 2-fold rotation of the 2D plane, since both can be

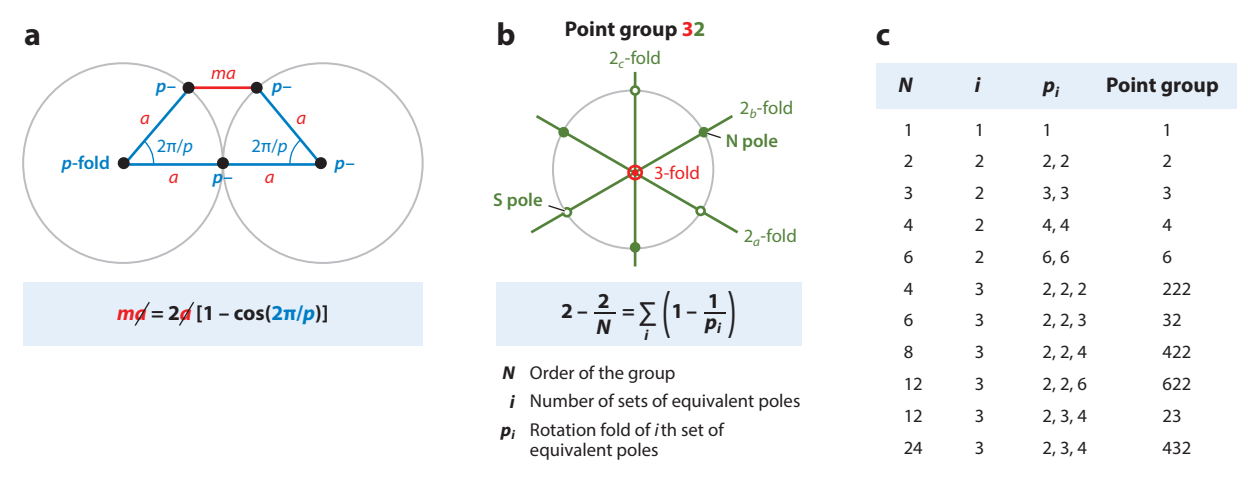


Figure 1

Derivation of rotational crystallographic point groups. (a) The crystallographic restriction theorem and a p-fold axis that periodically repeats every unit distance of a and requires the condition stated below, where m is a whole number. (b) The question of how many p-fold axes can pass through a single pivot point at the center of an imaginary sphere (gray circle) and still form a group describing the symmetry of a crystal placed at the pivot point. The example of the point group 32 is the set of elements $\{1, 3, 3^{-1}, 2_a, 2_b, 2_c\}$; here, N = 6 is the order of the group. Each axis has a north pole (N; filled green circles) and a south pole (S; open green circles), where the rotation axes and the sphere intersect. Equivalent poles can be moved into congruence with each other using elements of the group. (c) Table showing the 11 possible combinations of values of the variables that satisfy the equation shown in panel b and the corresponding point groups they correspond to. For the point group 32, i is equal to 3, corresponding to the three sets of poles (\circ , \circ , \circ), (\bullet , \bullet , \bullet), as shown, with $p_i = 2, 2$, and 3, respectively, for the folds of the axes corresponding to each set of equivalent poles.

represented by $(x \ y) \to (-x - y)$. In three dimensions, they are distinct, since $\bar{1}: (x \ y \ z) \to (-x - y - z)$, while the 2-fold transformation along the z-axis is $2_z: (x \ y \ z) \to (-x - y \ z)$. Rotoinversions combine rotation, R, with inversion, $\bar{1}$, to form the operation $R \cdot \bar{1} = \bar{R}$. This operation is distinct from R and $\bar{1}$, since an object can possess \bar{R} symmetry without possessing either R or $\bar{1}$. Rotations and rotoinversions of a periodic crystal that leave the crystal invariant together compose the 32 crystallographic point groups (14). When 3D translations in the Euclidean space are also included, the 32 point groups expand to 230 space groups, as listed in detail in the International Tables for Crystallography (15).

Neumann's principle states that the macroscopic properties of a material must at least possess the symmetry of its point group, thus intimately tying together symmetry and properties (2). Macroscopic means that the property in question is averaged over a sufficiently large number of unit cells for it to be insensitive to lattice translation symmetry. For example, if the point group of a crystal possesses inversion symmetry, $\bar{1}$, then all its macroscopic properties must at least possess inversion symmetry, thus ruling out macroscopic polarization such as ferroelectricity and pyroelectricity within this crystal. When microscopic properties involve unit cell translations, Neumann's principle needs to be restated as follows: Microscopic properties involving lattice translations of a material must at least possess the symmetry of its space group. For example, the arrangement of spins on different lattice sites related by translations determines the antiferromagnetic order (16, 17). Inversion symmetry is also useful in quantum mechanics; for example, one of the optical selection rules (18) states that dipole transition of electrons through a light field can occur only between two electronic states with opposite parities, namely, one state that is $\bar{1}$ -even (invariant under $\bar{1}$, such as s, d, and g orbitals) and another that is $\bar{1}$ -odd (reverses under $\bar{1}$, such as p, f, and b orbitals).

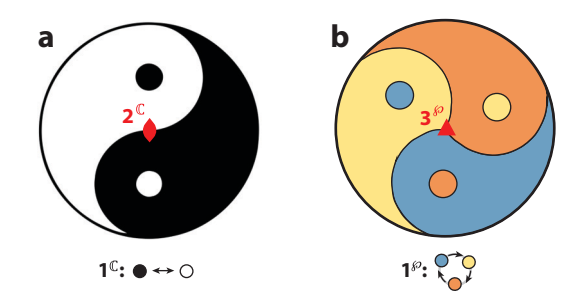


Figure 2

Color symmetry is illustrated with two-color and three-color objects. (*a*) If $1^{\mathbb{C}}$ is defined as an operation that exchanges black and white colors, then the yin-yang symbol in panel *a* is invariant under the symmetry operation $2^{\mathbb{C}}$, which is a 2-fold rotation followed by a color swap. (*b*) If $1^{\mathfrak{D}}$ is defined as an operation that cyclically permutes orange-blue-yellow colors, then the three-color symbol in panel *b* is invariant under the symmetry operation $3^{\mathfrak{D}}$, which is a 3-fold rotation followed by a three-color permutation.

2.2. Color Symmetry and Antisymmetry

Symmetry operations in the crystallographic point groups and space groups exclusively involve moving atoms around in 3D Euclidean space—that is, the spatial location of atoms. However, atoms also can possess other characteristics, such as type of chemical species, charge, and spin. These characteristics can be thought of as color in an abstract sense. If there are only two states of charge, say + or -, or only two states of quantum spin, say \uparrow or \downarrow , then we need only two colors to represent them. For example, we can use white for \uparrow and black for \downarrow . Two-color symmetries are called antisymmetries or anti-identities; an antisymmetry operation switches a black characteristic into a white characteristic or vice versa. **Figure 2** shows an example of a two-color and a three-color symmetry. Reviews on color symmetry by Lifshitz (19), Schwarzenberger (20), and Opechowski (21) are particularly recommended. This review solely focuses on two-color symmetries (antisymmetries). Permutation groups of three colors or more are distinct from the antisymmetry groups discussed in this review.

An antisymmetry with respect to a group can be defined (22) as an operation satisfying the following conditions: (a) It should be its own inverse (i.e., self-inverse), (b) it must commute with all elements of the group under consideration, and (c) it must not itself be an element of the group. By this definition, the spatial inversion operation is in fact an antisymmetry with respect to the group of proper rotations, SO(3). However, inversion is not an antisymmetry with respect to the Euclidean group E(3), since it does not commute with spatial translations.

A brief note on the history of antisymmetry is in order [see, e.g., articles by Zamorzaev (9) and Wills (23) and their bibliographies]. Heesch (22) introduced the idea of antisymmetry in 1930 and showed that color could be treated as a higher dimension. By including a single antisymmetry in the crystallographic groups, Heesch showed that they could be expanded into 122 point groups, now called Shubnikov groups. Zamorzaev (24, 25) extended these two-color point groups to two-color space groups, expanding the 230 crystallographic space groups to 1,651 two-color space groups. Landau & Lifshitz (26) reinterpreted black and white colors to correspond to time-reversal antisymmetry, 1', whose action reverses time; that is, $t \rightarrow -t$. These groups revolutionized the interpretation of neutron scattering from magnetic crystals and the interpretation of the magnetic properties of crystals, as long as the spins are treated classically. However, there are subtle conceptual issues in conflating time reversal with spin reversal, especially in quantum mechanics, which is discussed in Section 3.3. Gopalan & Litvin (27) introduced an antisymmetry named rotation-reversal symmetry in 2011 as a way to switch the sense of solid-body rotations of the rigid

polyhedra that compose a crystal. This idea was generalized to distortion-reversal antisymmetry, 1*, by VanLeeuwen & Gopalan (10) and VanLeeuwen (28) in 2015. It is shown in Section 4 to have important practical applications in predicting MEPs between an initial and a final state (10, 29, 30). Gopalan (11) introduced wedge reversion, 1[†], in 2019 as a missing antisymmetry in the classification of physical properties expressed as multivectors into eight principal and 41 overall types.

2.3. Antisymmetry Point Groups and Space Groups

Starting from 32 crystallographic point groups and 230 space groups, addition of antisymmetry operations expands the groups further. Consider including a single antisymmetry to the crystallographic groups, resulting in the so-called single antisymmetry point groups and single antisymmetry space groups. The most common application of these groups is in the form of 122 Shubnikov point groups and 1,651 space groups, all listed by Litvin (31, 32), where the antisymmetry is 1', the time-reversal operation. Of the 122 two-color point groups, 32 of them are colorless groups, the ones with no 1', and thus they are the conventional 32 crystallographic groups. Another 32 of them have 1' explicitly in them, and they are called gray groups—these groups cannot support a macroscopic magnetic moment, since Neumann's principle would require that the presence of a magnetic moment, M, will also require the presence of 1/M = -M in the system. Finally, there are 58 more where 1' is not present explicitly but is present in association with other rotation or rotoinversion operations, such as in, for example, $2' = 2 \cdot 1'$. These are called black-and-white groups. The colorless point groups (32 of them) and the black-and-white point groups (58 of them) can support a macroscopic magnetic moment, and hence, together they are called the 90 magnetic groups. Figure 3 gives examples of colorless, gray, and black-and-white single antisymmetry point groups.

If two antisymmetry operations are defined and represented as 1* and 1′, they can be used to generate double antisymmetry point groups and double antisymmetry space groups. In all, 17,803 possible double antisymmetry space groups and 624 double antisymmetry point groups exist, as listed by VanLeeuwen et al. (33). Huang et al. (34) published the complete symmetry diagrams for all of these groups. Padmanabhan et al. (35) listed all spatiotemporal point groups with time translations, and Liu et al. (36) listed all spatiotemporal point groups with time translations and time reversal. If time reversal is replaced by 1*, these listings would also apply to isomorphic distortion groups, described in Section 4. **Figure 4** shows example stereographic projections of double antisymmetry point groups. The addition of a third antisymmetry leads to 287,574 triple

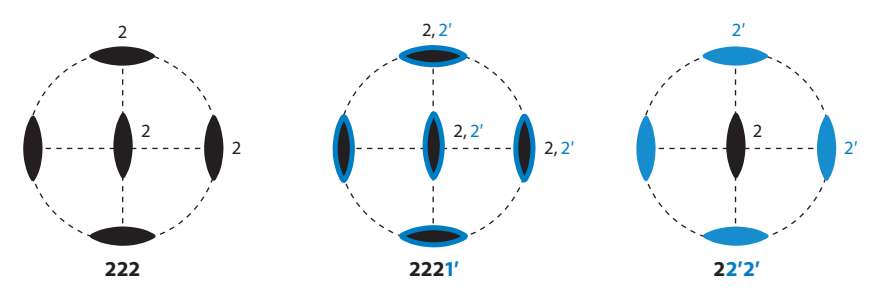


Figure 3

Stereographic projection of single antisymmetry point groups. The groups are denoted 222 (colorless), 2221′ (gray), and 22′2′ (black and white). The symmetry operations associated with 1′ are colored with blue. The complete listing of single antisymmetry point groups and single antisymmetry space groups is given by Litvin (31, 32).

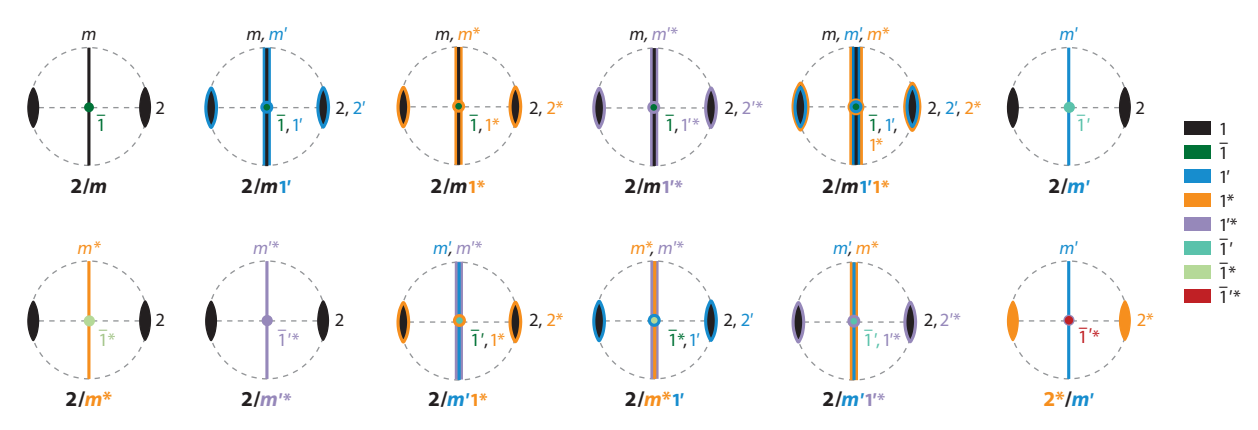


Figure 4

One example each of 12 types of double antisymmetry point groups when 1^* and 1' are combined with the crystallographic point groups. The symmetries 1, 1', 1^* , 1^* , 1^* , 1^* , 1^* , and $1^{'*}$ are shown; each antisymmetry is color coded as shown on the right. If space groups are considered, four of these symmetries involving 1^* would not be considered antisymmetries due to the presence of translations that do not commute with 1^* .

antisymmetry space groups (28) and 4,362 point groups (9); these are not yet explicitly listed. Beyond three antisymmetries, one can construct only gray point groups that explicitly contain the additional antisymmetry operations. This is because of a lack of greater than three distinct subgroups of index 2 (containing half the number of elements) of the original crystallographic point groups needed to construct black-and-white point groups.

3. TIME REVERSAL AS AN ANTISYMMETRY

Landau et al. (37) reinterpreted the generalized antisymmetry operation 1' as a time-reversal operation defined as follows: $1':t\to -t$. Classically, magnetic moments can be thought of as current loops, and hence, a time-reversal operation will flip the direction of the current in the loop and thereby flip the magnetic moment. Magnetic space and point groups, along with the advent of neutron diffraction, transformed the way magnetic materials and their properties were characterized. However, the above description of time reversal as an antisymmetry and its action on magnetic moments is valid only within a purely classical treatment of spin. The intrinsic spins of electrons are inherently quantum mechanical in origin and behave very differently from classical current loops, and care is needed in applying magnetic groups in these cases, as described in Section 3.3.

3.1. Neutron Diffraction Reveals Magnetic Symmetry

The antisymmetry operation 1' is used to reverse classical magnetic moments (equivalent to a flat current loop) between up (\uparrow) and down (\downarrow) states at each magnetic atom, while simultaneously leaving their spatial coordinates unchanged. The data in **Figure 5***a* are the first instance of the application of magnetic groups to neutron diffraction of a magnetic crystal (38, 39). Conventional X-ray photons do not distinguish between spin-up and spin-down electrons; they simply see the total electron density, $\rho_{\rm e}(r)$, and thus the scattering power is given by $f_{\gamma} \propto \rho_{\rm e}(r) = \rho_{\rm e}^{\uparrow}(r) + \rho_{\rm e}^{\downarrow}(r)$, where the superscripts indicate the two spin states. Neutrons scatter due to nuclear spin as well as the magnetic polarization of the electrons, namely, $f_{\eta^0}^{\rm mag} \propto \rho_{\rm e}^{\uparrow}(r) - \rho_{\rm e}^{\downarrow}(r)$, and hence can probe the underlying magnetic symmetry of the crystal. This was indeed observed with the first ever neutron diffraction experiment on MnO, performed by Shull & Smart (38) in 1949, which also

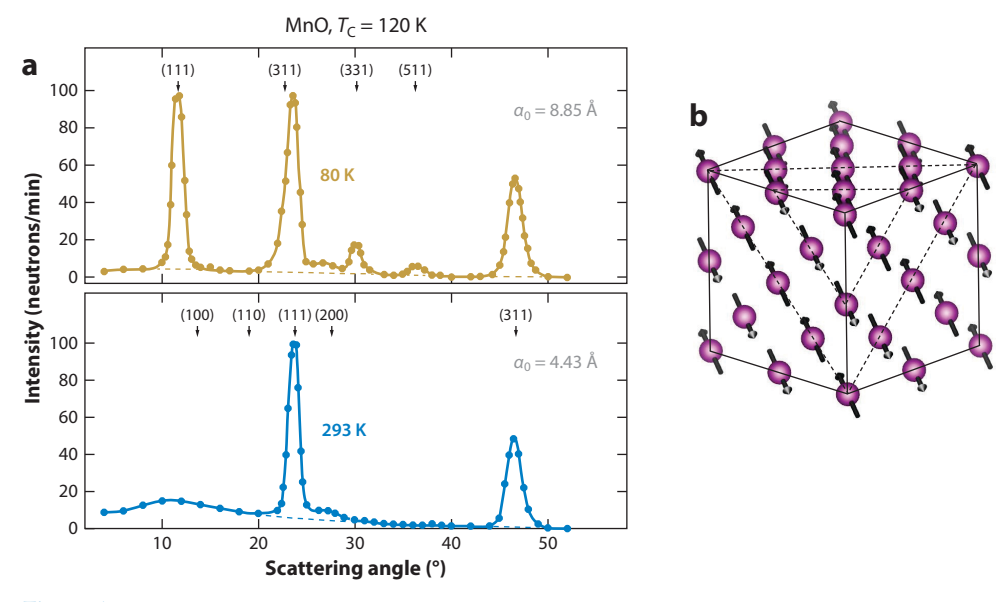


Figure 5

The first reported (39) neutron diffraction study on MnO, revealing magnetic symmetry. (a) Unit-cell doubling and four extra antiferromagnetic reflections are observed below the Néel temperature of 120 K, since neutrons are sensitive to the spin of the scattering electrons. (b) The unit cell of MnO, shown with only the Mn atoms and the magnetic moments at each site. The dashed lines show planes within which magnetic moments are aligned. Figure reproduced with permission from Reference 39; copyright 2019 American Physical Society.

happened to be the first direct evidence of antiferromagnetism, as shown in **Figure 5a**. To explicitly derive how the magnetic symmetry influences the neutron scattering in MnO, one first notes that the peak with the lowest scattering angle at 80 K is at half the scattering angle of that at 293 K, indicating doubling of the crystallographic unit cell caused by the magnetic structure of the antiferromagnetic phase. For X-ray diffraction, the scattering intensity at a wavevector difference of Δk is approximately given by $I_{\text{XRD}}(\Delta k) \propto |\Sigma_j f^j e^{-2\pi i r_j \cdot \Delta k}|^2$, where the summation is over the ions in the unit cell. Considering only the Mn atoms' lattice sites but ignoring their spins, this then evaluates to

$$I_{\rm XRD}\left(\Delta k\right) \propto \left|f^{\rm Mn} e^{-2\pi i \left(0\ 0\ 0\right)\cdot \Delta k} + f^{\rm Mn} e^{-2\pi i \left(\frac{1}{2}\ \frac{1}{2}\ 0\right)\cdot \Delta k}\right|^2,$$

which is nonzero when (b, k, l) for the diffracted planes are either all odd or all even; however, all-even indices are not experimentally observed above. For scattering of a neutron beam in the antiferromagnetic phase,

$$\begin{split} I_{\mathrm{ND}}\left(\Delta k\right) &\propto \left|f^{\mathrm{Mn}\uparrow}e^{-2\pi i(0\ 0\ 0)\cdot\Delta k} + f^{\mathrm{Mn}\uparrow}e^{-2\pi i\left(\frac{1}{2}\ \frac{1}{2}\ 0\right)\cdot\Delta k} \right. \\ &\left. + f^{\mathrm{Mn}\downarrow}e^{-2\pi i\left(\frac{1}{4}\ \frac{1}{4}\ 0\right)\cdot\Delta k} + f^{\mathrm{Mn}\downarrow}e^{-2\pi i\left(\frac{1}{2}\ 0\ 0\right)\cdot\Delta k}\right|^{2}, \end{split}$$

where $f^{\text{Mn}\uparrow} = -f^{\text{Mn}\downarrow}$ because of the interaction of neutrons with electron spins. The selection rules evaluate to (h, k, l) being all odd, as observed experimentally in **Figure 5***a*. The Bragg

diffraction of neutron beams at scattering angles that were believed to be forbidden according to the crystallographic space group symmetry $(Fm\bar{3}m)$ of MnO and its associated X-ray diffraction selection rules were actually allowed according to the magnetic space group $(C_{2c}2/m')$ of MnO.

3.2. Neumann's Principle Connects Magnetic Symmetry to Properties

In the context of magnetic properties such as magnetoelectricity and piezomagnetism (2), it is this magnetic symmetry that is of interest when applying Neumann's principle, stated in Section 2.1. To illustrate this, we consider the property of magnetoelectricity, $M_i = Q_{ij}E_j$, where M_i represents the components of the magnetization, an axial time-odd vector; E_j the components of the electric field, a polar time-even vector; and Q_{ij} the axial time-odd magnetoelectric second-rank tensor. By Neumann's principle, the magnetoelectric tensor vanishes if 1' or $\bar{1}$ is a symmetry element of the point group of a crystal (2). Thus, all 32 magnetic gray groups and 11 colorless groups with explicit inversion symmetry lack the magnetoelectric effect. The magnetoelectric effect was experimentally discovered for the first time (40) in chromium oxide; Cr_2O_3 with a magnetic point group of Cr_2O_3 is $\bar{3}'m'$. Neumann's principle implies then that $Q_{11}=Q_{22}$ and Q_{33} are the nonzero elements (the subscript 3 is along the 3-fold axis), both of which disappear above the magnetic transition temperature T_N (**Figure 6a**).

However, care is needed in applying 1' (41). For example, consider Ohm's law, $J_i = \sigma_{ij} E_j$, where i, j indicate Cartesian coordinates; J is the current density in angstroms per square meter, a time-odd vector; E is the electric field in volts per meter, a time-even vector; and σ is the electrical conductivity, a time-odd second-rank tensor. No magnetism is explicitly involved in this phenomenon, but time reversal is involved. From Neumann's principle, one would conclude for a paramagnetic metal that explicitly contains 1' as a symmetry element that $\sigma_{ij} = 0$, which is unphysical since paramagnetic metals are good conductors of electricity. The apparent contradiction is resolved by

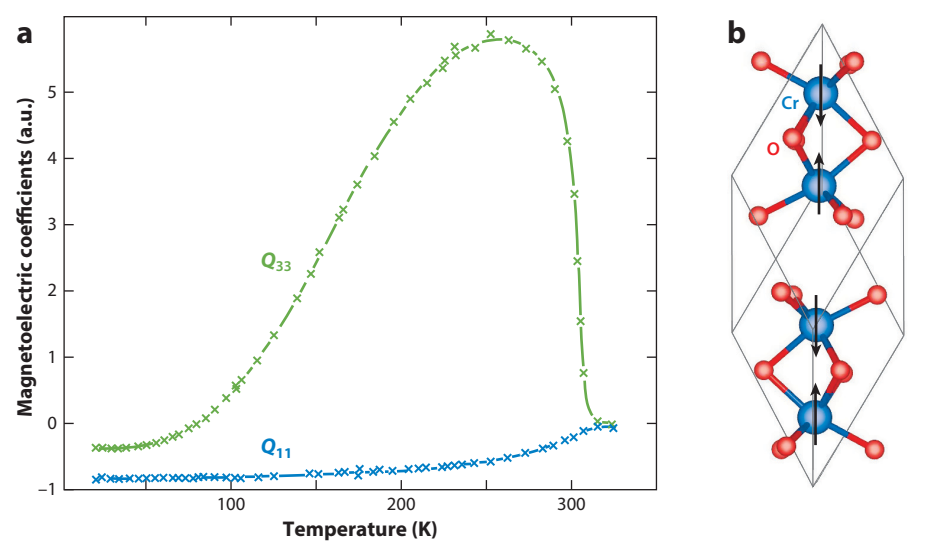


Figure 6

Magnetoelectric effect in Cr_2O_3 . (a) The first experimental discovery of the magnetoelectric effect, in Cr_2O_3 . The magnetic tensor coefficients Q_{11} and Q_{33} are plotted as a function of temperature. (b) The crystal structure of Cr_2O_3 ; the magnetic moments are shown as black arrows. Figure adapted with permission from Reference 40; copyright 2019 *Journal of Experimental and Theoretical Physics*.

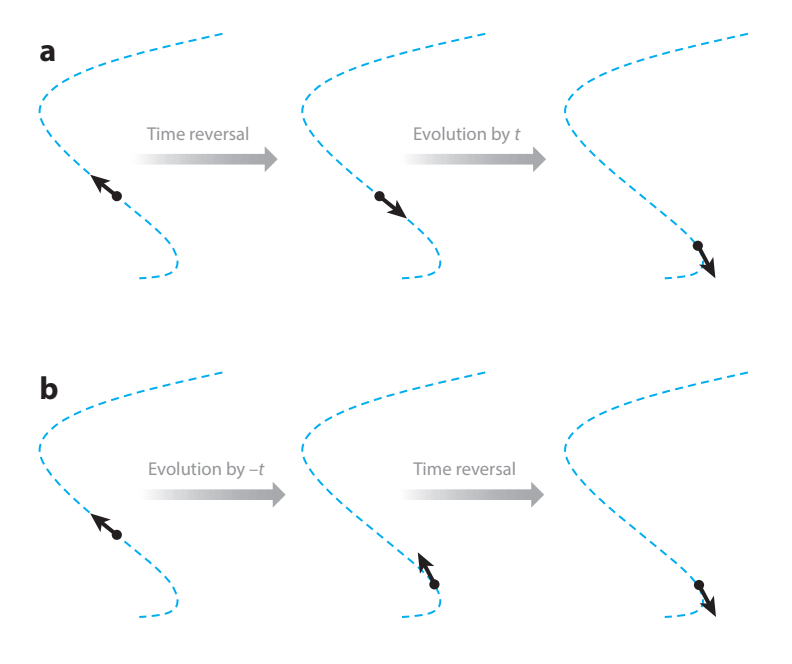


Figure 7

Illustration of classical time-reversal symmetry, \mathcal{T} . The figure shows that for a classical particle on a time-reversal symmetric trajectory, (a) applying the time-reversal symmetry operator first will cause the particle to reverse its momentum and retrace its trajectory, so that its new state after time t is identical to (b) that obtained by first propagating the particle by -t and then reversing its momentum. In other words, we obtain $\mathcal{T}(x(t), p(t)) = (x(-t), -p(-t))$.

noting that the current flow leads to energy dissipation through heat, which breaks time-reversal symmetry, 1'. In the well-known Hall effect (see 42), before applying a magnetic field, the longitudinal conductivity, σ_{ii} , is nonzero (due to dissipation), but the transverse conductivity, σ_{ij} , where $i \neq j$, is zero, suggesting that while longitudinal dissipation is significant, the transverse dissipation in these cases might be ignored since no work is considered done when the field and current are in orthogonal directions. In such cases, time-reversal 1' symmetry is preserved for the transverse conductivity but not for the longitudinal conductivity. However, when a magnetic field is turned on, 1' is broken, and a transverse Hall conductivity is also observed, as expected.

3.3. Time Reversal in Classical Versus Quantum Mechanics

As useful as it is to formulate time-reversal symmetry as an antisymmetry, 1', this is in principle valid only under a purely classical treatment of spins as loops of current. Laws of classical mechanics are invariant under the transformation $t \to -t$, whereas in quantum mechanics, time reversal additionally involves a complex conjugation operation (43). Furthermore, for quantum mechanics with half-integer spin systems, time-reversal symmetry is no longer even a self-inverse transformation, which is one of the requirements for an operation to be an antisymmetry (see Section 2.2). Nonetheless, magnetic space groups are in many cases applied to truly quantum mechanical phenomena (44). Below, we clarify these subtle issues.

First, following Wigner (45), we think of time-reversal symmetry as a reversal of the direction of motion. **Figure 7** depicts the action of an operator \mathcal{T} (it is identical to 1', used in crystallography) on position x and momentum p as follows: $\mathcal{T}(x(t), p(t)) = (x(-t), -p(-t))$. Laws of nature are

invariant under time-reversal symmetry, with some exceptions involving weak interactions in particle physics (46). For instance, $m\ddot{x} = F = -\nabla V(x)$ is invariant under time reversal, where V(x) is the potential associated with the conservative force F and where both x(t) and x(-t) are solutions. Maxwell's equations are also invariant under time reversal, if one considers the magnetic field \mathbf{B} to arise from moving charges or currents, so that $\mathbf{B} \to -\mathbf{B}$ under \mathcal{T} . Note that the operator \mathcal{T} is clearly an antisymmetry, since it is a self-inverse operator ($\mathcal{T}^2 = 1$) and commutes with rotations, rotoinversions, and translations.

We now consider time reversal in quantum mechanics. We first note that given the Schrödinger wave equation,

$$i\hbar\frac{\partial\psi}{\partial t} = \left(-\frac{\hbar^2}{2m}\nabla^2 + V\right)\psi,$$

for every $\psi(x,t)$ that is a solution, there exists another solution $\psi^*(x,-t)$. In fact, it can be shown (see **Supplemental Material Section S1.1** for a derivation), using the same recipe that was followed in **Figure 7** for a classical time-reversal symmetric trajectory, that given an eigenstate $\psi(x,t)$, the time-reversed eigenstate is given by $\psi^*(x,-t)$. It appears, then, that the time-reversal operator in quantum mechanics, labeled Θ here to make a distinction from the classical \mathcal{T} , is given by complex conjugation operation, K, along with time reversal, $\mathcal{T}: t \to -t$, that is, $\Theta = \mathcal{T}K$. We can quickly check that this formulation is consistent with the classical limit, where the momentum is reversed under time reversal, by noting that momentum eigenstates $|p\rangle = e^{-ip\cdot r}$ are transformed to $|-p\rangle = e^{ip\cdot r}$ under time reversal, so that the classical expectation value of momentum transforms as $p \to -p$. Note that $\Theta^2 = \mathcal{T}K\mathcal{T}K = 1$, since \mathcal{T} and K commute. This formulation of time reversal, namely, Θ , can thus be considered as time reversal in quantum mechanics formulations without spin-1/2 particles.

Strikingly, when quantum mechanical time reversal is applied to an electron, which is a spin-1/2 particle, it can be shown (see Supplemental Material Section S1.2 for a derivation) that time reversal is equal to $\Theta_S = \sigma_v K$, where the subscript S is for a spin-1/2 particle and σ_v is the 2 × 2 Pauli matrix $(0 - i; i \ 0)$. Noting that $K\sigma_v = -\sigma_v K$, it can now be shown that $\Theta_s^2 = \sigma_v K \sigma_v K = -1$. Therefore, if we apply time reversal twice on, say, a spin-up particle in a state $|\uparrow\rangle$, we obtain $\Theta_S^2|\uparrow\rangle = -|\uparrow\rangle$, and likewise, with a spin-down particle, we obtain $\Theta_S^2|\downarrow\rangle = -|\downarrow\rangle$. This is a radical departure from what is expected from classical current loop magnetic moments, but one with important consequences that are ubiquitous in quantum mechanics. The most prominent example is that of the Kramers theorem (47–49), depicted in Figure 8, which states that for every Bloch state $|\psi_k\rangle$ in a crystal with spin \downarrow and energy ϵ_k , there exists an orthogonal eigenstate $\Theta_S|\psi\rangle$ with spin \uparrow and the same energy, ϵ , i.e., $\epsilon_{k,\uparrow}^m = \epsilon_{-k,\downarrow}^m$, where k is the particle wavevector and the superscripts indicate two different energy bands m and n. The band structure is thus symmetric about k = 0. Another consequence is that the eigenstates at time-reversal invariant momenta k = 0 and $k=\pm\pi/a$ are 2-fold degenerate. Members of this subset of k points are deemed time-reversal invariant momenta, because applying the time-reversal operation Θ leaves each of them completely invariant to within a reciprocal lattice vector G, that is, $k \stackrel{\Theta}{\to} -k = k + G$. Kramers degeneracy can be broken by breaking time-reversal symmetry, such as by applying an external magnetic field **B**.

Now we go back to our original question. It appears, on the basis of the result $\Theta_S^2 = -1$ for spin-1/2 particles, that Θ_S is no longer a self-inverse operation; can it then be still treated as an antisymmetry? In both quantum and classical mechanics, we can think of the time-reversal operator as flipping the sense of rotation of the tiny current loops, which defines the electron spin; that said, the associated quantum phase that is inherited in the time-reversal operation can have physically meaningful results, such as in the Aharonov-Bohm effect (50). Separately, it is easy

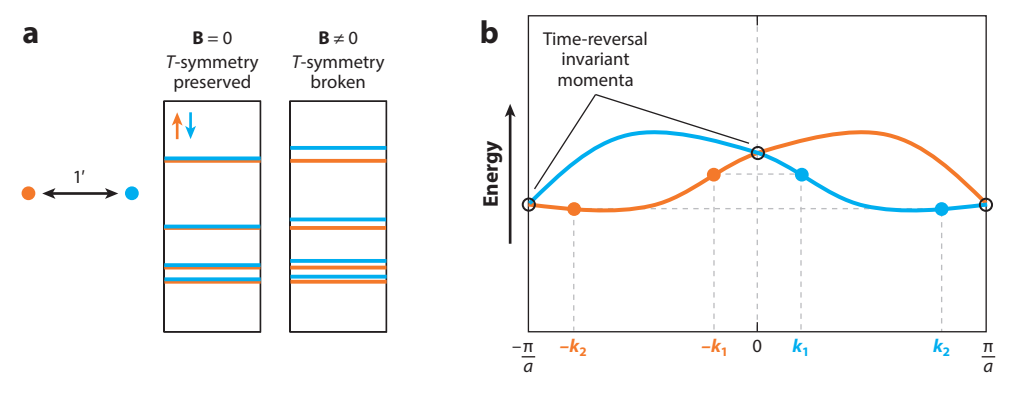


Figure 8

Illustration of time-reversal symmetry and Kramers degeneracy. (a) The eigenstates of a spin-1/2 particle when time-reversal symmetry is present ($\mathbf{B}=0$) and when it is broken ($\mathbf{B}\neq0$). The eigenstates are necessarily 2-fold degenerate in the presence of time-reversal symmetry. (b) A band structure in the presence of time-reversal symmetry. Kramers degeneracy implies that eigenstates at \mathbf{k} and $-\mathbf{k}$ are degenerate, time-reversal symmetric pairs, so that the band structure is symmetric about $\mathbf{k}=0$. Another consequence is that the eigenstates at time-reversal invariant momenta $\mathbf{k}=0$ and $\mathbf{k}=\pm\pi/a$, shown with open circles, are 2-fold degenerate.

to show (see **Supplemental Material Section S1.3**) that as long as one considers only expectation values of operators, rather than off-diagonal matrix elements, the classical time-reversal operator \mathcal{T} and quantum mechanical time-reversal operator Θ will give the same result. It can also be shown (51) that in the absence of spin-orbit coupling, Θ can be assumed to be simply K even for a spin-1/2 particle. Clearly, $\Theta_S = K$ is a self-inverse operation, since $K^2 = 1$. It is in these limits that the formulation of 1' as an antisymmetry, and the associated magnetic space groups, is valid in the study of quantum phenomena as well. Further, instead of representation theory, we must use corepresentation theory that is suitable for antiunitary groups, a discussion of which is covered in detail by Bradley & Cracknell (51) and is beyond the scope of this review.

4. ANTISYMMETRY OF DISTORTIONS

A recent application of antisymmetry in materials research comes in the form of distortion-reversal antisymmetry, 1*, which reverses the atomic trajectories that compose an arbitrary distortion. Consequently, a symmetry-based description of a wide range of phenomena—including atomic diffusion, vibrations, phase transitions, interface dynamics, and ferroelectric and magnetic switching—is enabled.

Distortion reversal traces its origin to the rotation-reversal antisymmetry operation, 1^{Φ} , proposed by Gopalan & Litvin (27) in 2011, as illustrated in **Figure 9**. Gopalan & Litvin identified an empty entry in **Figure 9a** and proposed to place 1^{Φ} there to reverse time-even axial vectors. It was introduced to reverse the sense of rotations of the polyhedra composing a crystal, between clockwise $(-\Phi)$ and counterclockwise $(+\Phi)$ directions about the center of mass of each polyhedron, that is, $1^{\Phi}: \Phi \to -\Phi$. This is shown schematically in **Figure 9b,c**, with polyhedra rotated both clockwise and counterclockwise by an angle Φ . The antisymmetry operation was conceived as reversing the sign of Φ , namely, $1^{\Phi}: \Phi \to -\Phi$. Thus, this structure is identified to have a colorless point group symmetry of mm^2 , and a color symmetry of $4^{\Phi}_z m_x m^{\Phi}_{xy}$. Examples of applications include rotations of O_6 oxygen octahedra in complex oxides (52) and SiO₄ tetrahedra in silicate structures such as quartz (53). However, VanLeeuwen (28) identified the difficulty in uniquely

Supplemental Material >

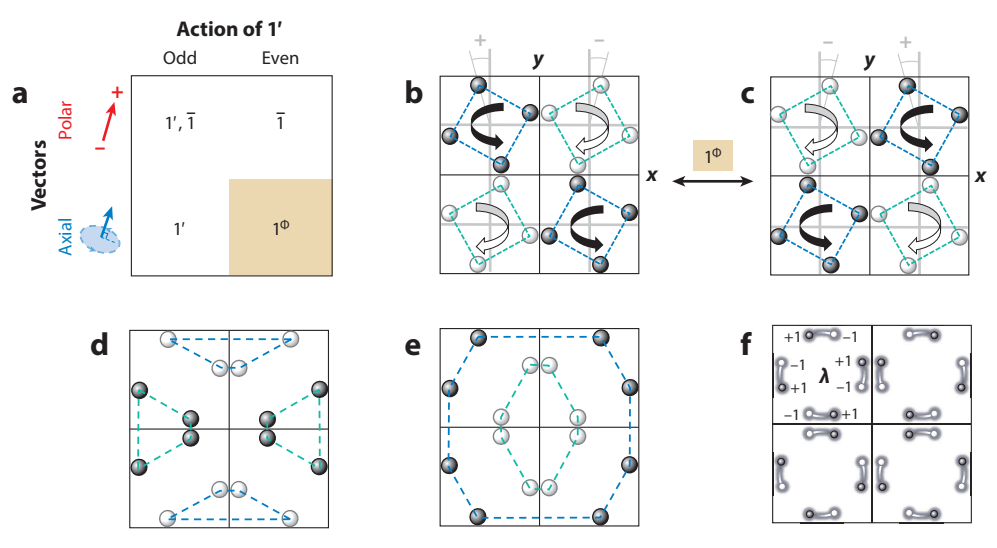


Figure 9

Illustration of the rotation-reversal antisymmetry operation, 1^{Φ} . (a) If the action (even or odd) of time reversal, 1', on two types of vectors, polar and axial, is considered, one can place antisymmetry operation entries in each box that will reverse the corresponding vector. (b,c) In this example illustrating the action of 1^{Φ} on a collection of atoms represented by white and black circles, the atoms are all identical, but the black and white colors highlight the color symmetry. (d,e) A problem with the conceptual implementation of 1^{Φ} is that, when a different selection of polyhedral units is used, the action of 1^{Φ} will no longer be a pure rotation but a general distortion. (f) A general distortion can be parameterized by a dimensionless parameter, $-1 \le \lambda \le 1$, and reversed by a distortion-reversal antisymmetry, 1^* : $\lambda \to -\lambda$.

identifying polyhedra in solids, as illustrated in **Figure 9***d*, *e*. In addressing these shortcomings, the idea arose of distortion-reversal symmetry, 1*, proposed by VanLeeuwen & Gopalan (10) in 2015. If the trajectories of atoms are deterministically tracked in the distortion process, and all polyhedral identification is dropped, then the distortion can simply be considered as a collection of trajectories of each atom, as shown in **Figure 9***f*. Each trajectory can be parameterized by a dimensionless parameter, $-1 \le \lambda \le 1$, where -1 and +1 represent the two extrema of each trajectory. This is described in detail in the next section. A similar concept, called choreographic symmetry, was proposed by Boyle et al. (54) in 2016, but it is not reviewed here separately.

4.1. Distortion-Reversal Antisymmetry, 1*

To fix the arbitrary nature of choosing polyhedra and rotation angles, one should first avoid the need for any polyhedral identification in a solid and directly work with the atoms and their atomic trajectories involved in a distortion. A general distortion, whether a rigid body rotation, a translation, a scaling, or a general deformation involving changes in internal angles, can then be described by a collection of atomic trajectories, as shown in **Figure 9f**. By parameterizing the atomic trajectories traced out with a reaction coordinate (λ), an antisymmetry operation acting on λ can be defined as distortion-reversal antisymmetry: $1^*: \lambda \to -\lambda$; it reverses the individual atomic trajectories that make up the pathway of the distortion. Since λ is a general reaction coordinate, many different aspects of a system can be used to parameterize with it.

Figure 10 illustrates a simple example of a ball rolling down a hill, where its height is used to parameterize the process linearly with λ . Here, the top of the hill (initial state) is at $\lambda = -1$ and the

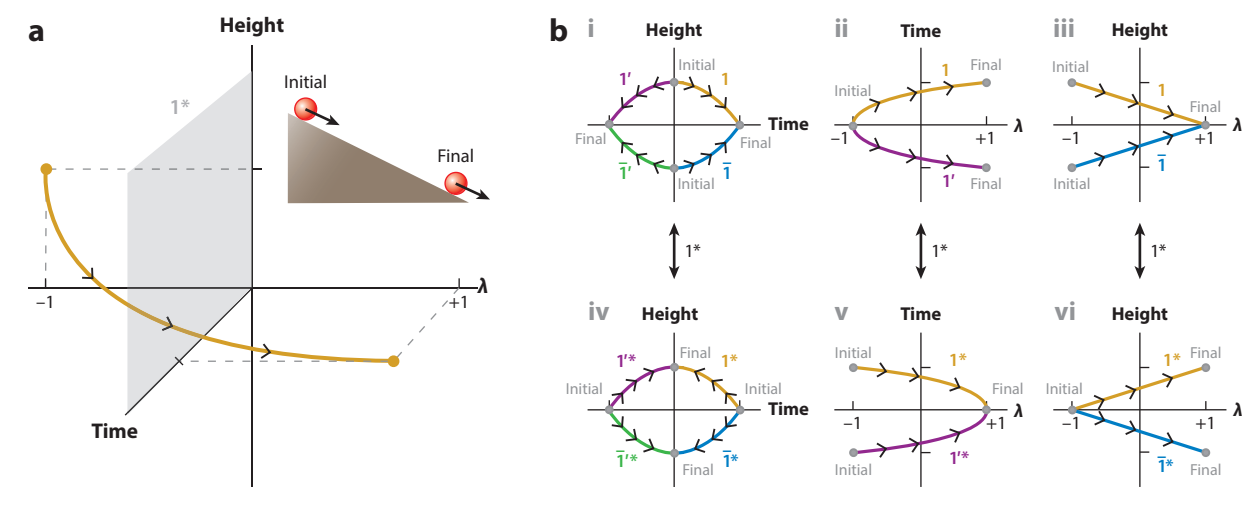


Figure 10

Illustration of distortion-reversal antisymmetry, 1^* . (a) Parameterization of a path taken by a ball rolling down a hill (*inset*), with the height used to generate a linear reaction coordinate λ between -1 (initial) and +1 (final) states, which acts as a time-like coordinate. (b) Illustration of how both time-reversal and distortion-reversal operations transform the pathway taken by the ball in panel a. The actions of elements of the group $\{1, \bar{1}, 1', 1^*, \bar{1}', \bar{1}^*, 1'^*, \bar{1}'^*, \bar{$

bottom of the hill is at $\lambda = +1$. In this example, it is important to note that λ evolves quadratically with time (t) as the ball accelerates down the hill due to gravity. Both 1' and 1* for this process act in different spaces, respectively, reversing the time (t) and time-like (λ) coordinates independently. Conventionally, $\lambda = -1$ is taken as the initial state and $\lambda = +1$ as the final state. Under the action of 1*, the initial and final states are reversed.

4.2. Distortion Symmetry Groups Uniquely Tag a Distortion Path

The antisymmetries 1* and 1' can be combined with the 32 crystallographic point groups and 230 space groups to form 624 double antisymmetry point groups and 17,803 double antisymmetry space groups (see Section 2.2). Of these, the groups that do not explicitly contain 1* (nongray groups) were named by VanLeeuwen & Gopalan (10) as distortion symmetry groups; this is in analogy with the magnetic groups that do not contain 1' explicitly. These consist of a set of elements that leave a whole path invariant when applied to its atomic trajectories. Consequently, it is the collective symmetry of an entire path instead of the symmetry of the individual frames (or images) within the path. Distortion symmetry groups are useful in finding MEPs between an initial and a final state of a material system. This first requires determining the distortion symmetry group of an initial path.

To tag a path with a unique distortion group, G, we first determine the group of unstarred symmetry operations (ones that do not have any association with the distortion-reversal operation, 1^*) that leave the whole path invariant. This group (H) can be obtained through an intersection of the conventional crystallographic symmetry groups $S(\lambda)$ of each frame λ in a path—that is, $H = \bigcap_{1 \le \lambda \le 1} S(\lambda)$ —that ranges by convention, as stated above, from $\lambda = -1$ to $\lambda = +1$. From here on, a set of elements in S(0) are identified (called A) that map the system at λ to $-\lambda$. When combined with 1^* , that is, 1^*A , the new elements generated will be symmetries of

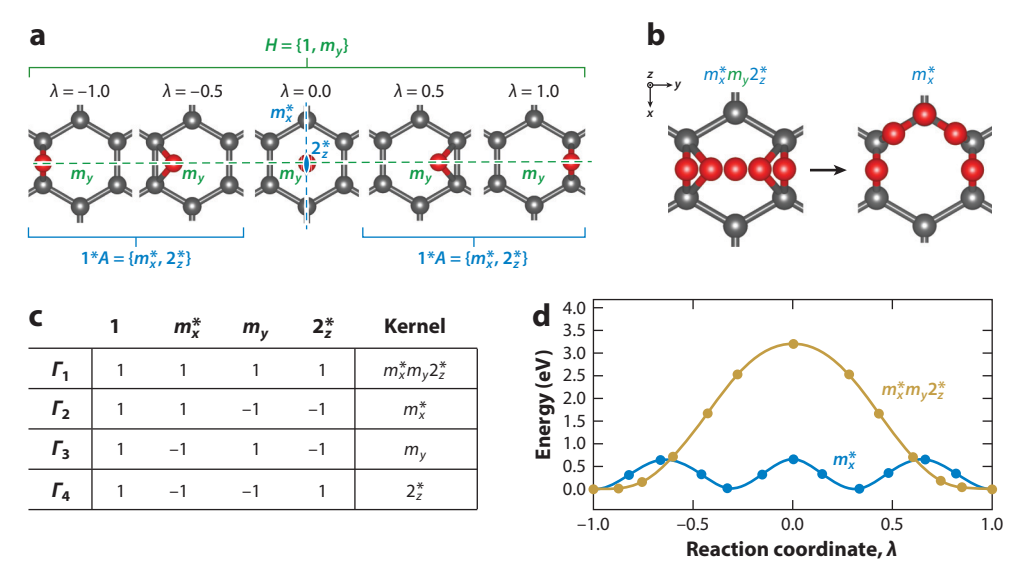


Figure 11

The distortion symmetry group helps determine the minimum energy pathway for the diffusion of oxygen across a carbon ring in graphene. (a) The elements of unstarred (group H) and starred (set 1*A) symmetry elements are shown. (b) Taking the union of both sets of elements gives the distortion group of m*m2* for the initial path shown here. An exaggerated version of the symmetry-adapted perturbation used to lower the path symmetry to m* is also shown. (c) The character table of m*m2* shows the four irreducible representations that define the four unique perturbations to the initial path. (d) Applying these perturbations to the nudged elastic band method yields the result that the minimum energy pathway is m*. Further perturbing the minimum energy pathway by treating it as the initial path and performing the same procedure as on m*m2* does not lower the energy barrier any further (10).

the path. The elements of the overall distortion group G of the entire path can then be obtained as $G = H \cup 1^*AH$. Figure 11 illustrates obtaining the distortion group for the path of an oxygen atom diffusing across a graphene surface. Additionally, since one has control in choosing the initial path in finding an MEP, it can be highly symmetrized by choice in order to take full advantage of distortion symmetry and group theory; one can systematically lower the symmetry with group-theory-dictated perturbations and find many intermediate paths starting from a single path.

4.3. Finding Minimum Energy Pathways by Using Distortion Symmetry Groups

Distortion groups have recently been demonstrated to be a powerful tool for finding the MEP, identified as the lowest energy path for the distortion (rearrangement) of a group of atoms from an initial stable state ($\lambda = -1$) to a final stable state ($\lambda = +1$). The reaction coordinate here is thus λ , whether it is temperature, pressure, stress, electric or magnetic field, or any other intensive parameter in response to which the system changes state. The potential barrier maximum then corresponds to a saddle-point energy that determines the transition rate within the harmonic transition state theory (55).

There are infinitely many paths from an initial to a final state in the phase space of intensive parameters. Determining the MEP from among them is thus a central problem in all of materials science, chemistry, physics, and biology. Of the many methods (56, 57) that are used to find an MEP [instead of the MEP, since the nudged elastic band (NEB) method cannot ensure a global minimum but only a local minimum] starting from an initial guess path, the NEB method is one

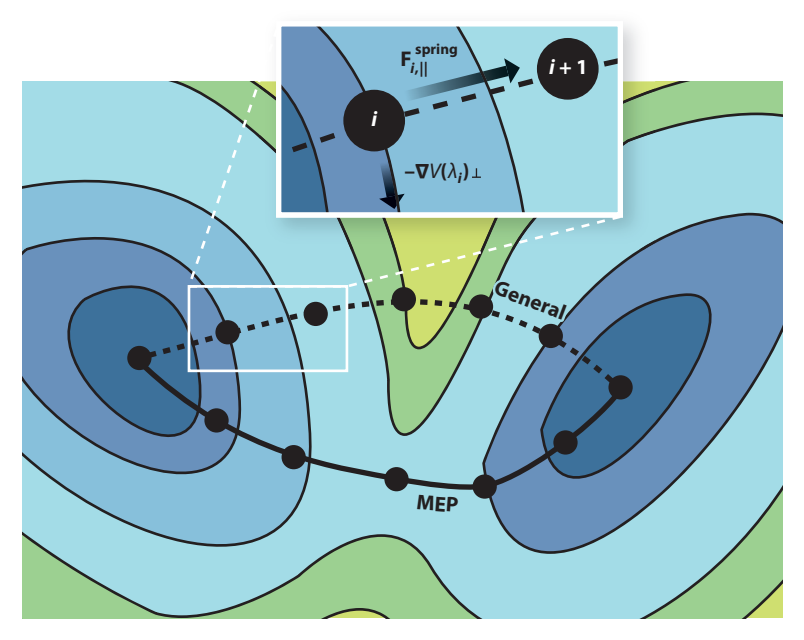


Figure 12

Schematic illustrating the nudged elastic band method to find the minimum energy pathway (MEP) between two low-energy valleys. The background is the potential energy (V) surface plotted as a colored contour plot, with the black contour lines representing isoenergy lines. The blue end of the color spectrum represents low energy and the yellow end high energy. Two paths are illustrated: The one with a dashed black line is a general path, and the one with a solid black line is the MEP. The black filled circles represent some intermediate images (labeled i in the imset) along the two paths, parameterized by a value of λ between -1 (initial state) and +1 (final state) for the respective paths. The inset shows a force component parallel to the path, due to the spring, and a force component perpendicular to the path, due to the potential energy surface.

of the most common (58-60). The essential idea is depicted in Figure 12. The NEB method is a chain-of-states method, where an initial guess path between the initial and final states is defined by a series of intermediate frames (called images), which are artificially connected by springs of some stiffness (not shown) to keep them uniformly apart along the path. This in turn allows for the parameterization of the images with a uniformly distributed λ . In the NEB method, the forces on these images are then put through a projection scheme such that the (artificial) spring forces perpendicular to the path $(\mathbf{F}_{\perp}^{\text{spring}})$ and the component of the true force (equal to the gradient of the energy potential) parallel to the path (i.e., $-\nabla V_{\parallel}$) are zero; this process is called nudging. Thus, in a path, the surviving force on any image i is given by $\mathbf{F}_i^{NEB} = -\nabla V(\lambda_i)_{\perp} + \mathbf{F}_{i,\parallel}^{\text{spring}}$. From here, an optimization scheme can be employed to move the images along \mathbf{F}^{NEB} and try to converge to an MEP. The process of finding the true MEP is, however, stochastic, relying on guessing as many initial starting paths as possible and comparing their NEB-optimized MEPs to find the most likely MEP. No symmetry principles are used in the NEB method or in any other numerical method to find MEPs. Lack of numerical convergence in running NEBs also results in one never being sure whether a final MEP is correct or even properly converged (see examples in 10, supplementary information).

Distortion symmetry allows for tagging each possible distortion path with a unique distortion group (Section 4.2). Further, when we pick an initial path and determine its distortion group, group theory tells us the number of irreducible representations (irreps) in that group. Each 1D irrep

represents a unique way to perturb the initial path, and each irrep is orthogonal to the others. Irreps with n dimensions will produce n perturbation vectors. In this manner, there are a finite number of distinct ways to perturb an initial path, as determined by the distortion group and its group theory representation. Each irrep can then be used to perturb the initial path and lower its distortion symmetry systematically (29, 30). Once an MEP is found, its distortion group will determine the unique number of ways to perturb that path further. Once a true (local) MEP is found by the NEB method, any further perturbations based on its irreps will not lower the symmetry of the path any further. This is because the distortion symmetry of a path can be unchanged or raised by the NEB calculation, but never lowered (10). In other words, if S is a symmetry of a path P—that is, if SP = P—then S[NEB(P)] = NEB(P).

4.4. DiSPy: Distortion Symmetry Method Implemented in Python

The above procedure has been deemed the distortion symmetry method and has recently been implemented into a Python package (DiSPy) by Munro and coworkers (30) and applied to the study of vibrations, diffusion (10), and ferroelectric switching (29). In the process, it was demonstrated how the tool can enable previously overlooked switching pathways to be discovered, as well as allow for the exploration of the potential energy landscape around an initially chosen highly symmetric path.

The DiSPy package works by using projection operators to generate symmetry-adapted perturbations from what would be an arbitrary perturbation to an initial path. This is effective because the goal of any path perturbation is to invoke unstable modes of an initial path that may exist to lower its symmetry. Since these unstable displacive modes necessarily transform as irreps of the path's distortion symmetry group, access to them is granted through the use of these operators. More specifically, individual displacive modes can be generated with projection operators that form a basis for any stable or unstable displacive mode that transforms as that same irrep. Perturbing with these can then be used to push a path along its instabilities without having to directly calculate the modes associated with them. This is advantageous, as this type of calculation for many systems would be computationally expensive to perform. More specific details on the theoretical background of the method can be found in the resource by Munro and coworkers (30). The goal of the DiSPy package is to make it easy to generate symmetry-adapted perturbations as described above. The package is written to use the input and output capabilities included in the pymatgen package (61), thus accommodating a large variety of formats for many electronic structure and molecular dynamics packages.

4.5. Examples of Minimum Energy Pathways Using the Nudged Elastic Band Method Plus Distortion Symmetry

The above approach can be applied to the diffusion example shown in **Figure 11**. If the NEB algorithm is run using the linearly interpolated path (**Figure 11**a), a high-energy pathway is obtained (**Figure 11**d). Using DiSPy, this relaxed path can then be perturbed with symmetry-adapted perturbations constructed using the irrep matrices shown in the character table of m^*m2^* (**Figure 11**c). By using the perturbation associated with the Γ_2 irrep, a lower-energy path with a distortion symmetry of m^* is found if the NEB algorithm is run again. This lower-energy path instead consists of the oxygen diffusing along the edge of the carbon ring instead of across it. Perturbations generated with the other two nontrivial irreps simply cause NEB to return back to the high-energy linearly interpolated path. In other words, they are stable perturbations.

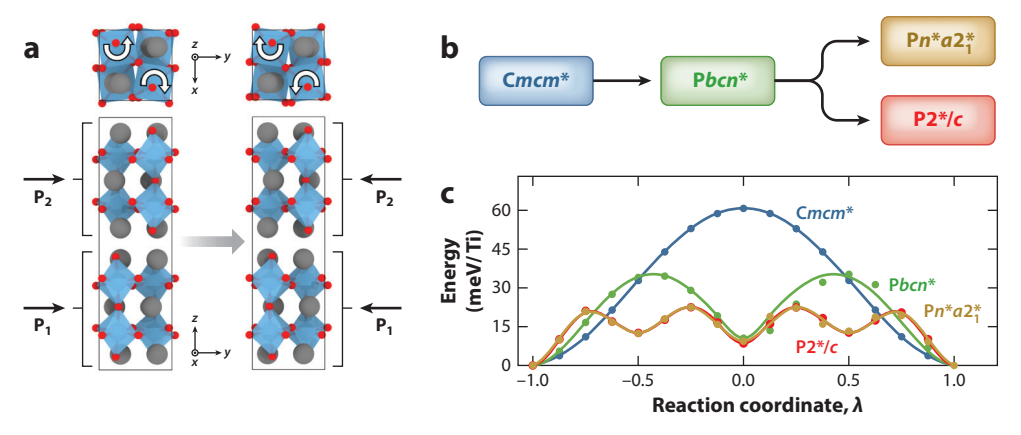


Figure 13

(a) The initial and final state of ferroelectric switching in Ca₃ Ti₂O₇. The polarization **P** in each layer is shown with black arrows. Ca, Ti, and O are indicated by gray, blue, and red atoms, respectively. (b) Flowchart showing the tree of symmetry-adapted perturbations and the resulting distortion symmetry group of the path. The initial linear interpolated path between the end states has a distortion symmetry group of Cmcm*. (c) The energy profiles for the paths obtained after applying the perturbations and running the nudged elastic band algorithm. The blue curve corresponds to that for a linear interpolated path between the initial and final structures. A previously reported (62) lower-energy two-step path is shown in green. Two of the new lower-energy four-step paths are shown in red and tan and result from perturbing the two-step path (29). Figure adapted with permission from Reference 29; copyright 2019 American Physical Society.

The distortion symmetry method (using the DiSPy code) was applied to the study of ferroelectric switching in Ca₃Ti₂O₇, an improper ferroelectric; PbTiO₃ and LiNbO₃, proper ferroelectrics; and BiFeO₃, a multiferroic (29, 30), For Ca₃Ti₂O₇ and BiFeO₃ in particular, lowenergy switching pathways were discovered beyond those reported in the literature through the use of conventional approaches with NEB calculations (62, 63). In Ca₃Ti₂O₇, six new four-step paths were found that pass through previously known low-energy orthorhombic and monoclinic phases of the material (Figure 13) (29). In BiFeO₃, switching involving both the polarization and magnetization was explored, defining two different kinds of paths—those that switch only the polarization but not the magnetization, and those that switch both. As a result, it was shown how the polarization of the material could be reversed without reversing the net magnetization, at a similar energetic cost to the process when both are reversed (29). This informs studies where deterministic switching of the net magnetization through control of the polarization is sought (64). Interestingly, the newly discovered low-energy path was also found to have a unique intermediate metastable structure where the polarization and magnetization in the BiFeO3 were aligned parallel or antiparallel to each other; normally they are perpendicular to each other in the ground state (65).

If the initial guess path for NEB is selected to be one with a very high degree of symmetry, many different symmetry-adapted perturbations can be calculated and used to explore a large number of potential pathways. An example of this is given by the study on pathways for domain wall motion in PbTiO₃ (29). The distortion symmetry method was used to obtain many different pathways between the two end states, and the polarization at the domain wall was calculated as a function of the reaction coordinate for each of the paths. Unlike the classical expectation of Ising ferroelectric walls, finite Bloch and Néel components (66) of polarization arose in many of the newly obtained paths.

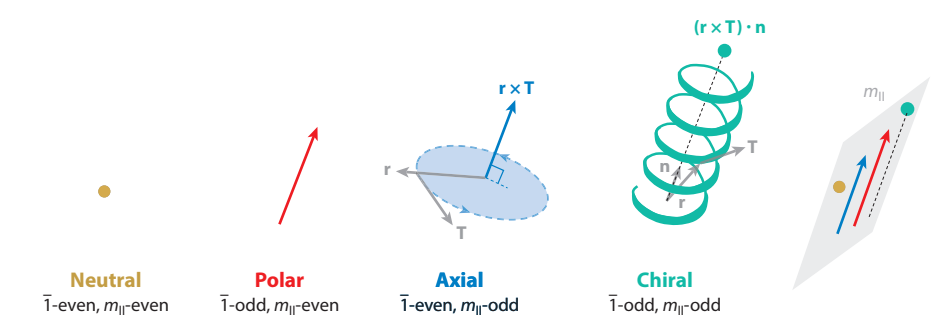


Figure 14

Four primary types of vector-like objects in three dimensions classified by Hlinka (67). In three dimensions, these are, respectively, a scalar (neutral), a polar vector (polar), an axial vector (axial), and a pseudoscalar (chiral). The transformation of these four objects under spatial inversion, $\bar{1}$, and a mirror, m_{\parallel} , defined by Hlinka is indicated below each object (even means invariant action; odd means the sign is reversed under the action of the relevant symmetry operation indicated). The 2D mirror plane operation, m_{\parallel} , was defined by Hlinka as parallel to the scalar or to the axes of the other objects and is schematically depicted on the far right. Each of these objects can further be time-even (invariant under the action of time reversal, 1') or time-odd (reversed under the action of 1'), giving rise to a total of eight types of vector-like objects.

5. ANTISYMMETRY-BASED CLASSIFICATION OF MULTIVECTORS

5.1. Current Classification of Vector-Like Quantities in Three Dimensions

Can we classify all (nonrelativistic) physical quantities in arbitrary dimensions? Physical quantities are typically represented in terms of scalars, vectors, and tensors of various types, collectively called vector-like quantities by Hlinka (67). **Figure 14** depicts eight types of vector-like objects in three dimensions as classified in Reference 67:

- 1. neutral (scalars) of two types, time-even (such as charge, *q*, or length, *r*) and time-odd (such as time, *t*);
- polar (vectors) of two types, time-even (such as position vector, r) and time-odd (such as velocity vector, v);
- 3. axial (vectors) of two types, time-even (such as a polarization loop, $\mathbf{r} \times \mathbf{P}$) and time-odd (such as current density loop, $\mathbf{r} \times \mathbf{J}$), where \mathbf{r} is the radius vector of the loop and \mathbf{P} and \mathbf{J} are tangential polarization and current density vectors, respectively, around the perimeter of the loop; and
- 4. chiral vectors of two types, time-even [such as helical winding, $(\mathbf{r} \times \mathbf{T}) \cdot \mathbf{n}$] and time-odd [such as current moving through a solenoid, $(\mathbf{r} \times \mathbf{J}) \cdot \mathbf{n}$], where \mathbf{r} , \mathbf{T} , and \mathbf{n} are, respectively, the radial, tangential, and axis vectors of the helix as shown in **Figure 14**.

In Hlinka notation, these four objects would respectively be named N, P, G, and C for time-even and L, T, M, and F for time-odd objects. Note that axial vectors (also called pseudovectors in three dimensions) can be written as cross products between two polar vectors or two axial vectors. The chiral vectors are really pseudoscalars in three dimensions and involve a dot product between an axial and a polar vector. **Figure 14** also indicates the transformation of these objects under $\bar{1}$, 1', and a mirror plane m_{\parallel} in 3D space defined in Reference 67. Here time-even refers to invariance under time reversal, 1', and time-odd refers to reversal of the object or quantity under 1'. Similarly, $\bar{1}$ -even is termed centric, and $\bar{1}$ -odd is termed acentric.

5.2. Transitioning from Three Dimensions to n Dimensions by Using the Language of Multivectors

Note that the above quantities—q, r, $r \times T$, $(r \times T) \cdot n$ —depicted in Figure 14 are composed of zero, one, two, and three vectors, respectively. One could continue to define more physical quantities composed of an even larger number of vectors, and thus an infinite sequence of quantities could be composed as scalar, S (grade 0, composed of no vectors); vector, V (grade 1, composed of one vector); bivector, B (grade 2, composed of two vectors); trivector, T (grade 3); quadvector. Q (grade 4); pentavector, P (grade 5); and so on for a general blade (of grade g, composed of g vectors), as they are called in Clifford algebra (CA) (see Supplemental Material Section S2.1 for a brief introduction to CA). In addition, CA allows the addition of such blades, for example, M = S + V + B + T + Q + P, etc., which is an arbitrary multivector living in a 2⁵-dimensional CA space arising from a five-dimensional vector space. For example, in CA, the electromagnetic field F is a multivector defined as F = E + cB, where E is the electric field vector and B is the magnetic field bivector. Similarly, the current density $J = (\rho/\epsilon_0) - \epsilon \mu_0 J$ is a multivector (ρ is charge density, c is the speed of light in vacuum, ε_0 is permittivity, and μ_0 is the permeability of free space). CA allows one to write all four of Maxwell's equations in free space succinctly as one single equation, $[\nabla + (1/\epsilon)\partial/\partial t]F = J$, in Newtonian space plus scalar time, t, a process called encoding that reveals deeper interconnections between diverse laws (13, 68).

This may seem unusual at first, because one is typically more conversant with physical properties being conventionally represented in the language of tensors of different ranks, such as scalars (rank 1), vectors (rank 1), and tensors of ranks 2, 3, 4, ..., etc. Further, adding scalars to vectors and tensors of higher ranks is unusual. One can, however, show that most of the physically relevant tensors can be written as multivectors, and hence the language of multivectors is an alternate representation of tensors, but with the advantage of being coordinate-free (69, 70). As a simple example, consider a rank 2 tensor property, T_{ij} , in two dimensions spanned by unit vectors $\hat{\mathbf{x}}$ and $\hat{\mathbf{y}}$, which thus has four independent terms, T_{11} , T_{12} , T_{21} , and T_{22} . One can write this tensor as a multivector M, where $2M = (T_{11} + T_{22}) + (T_{12} + T_{21})\hat{\mathbf{x}} + (T_{11} - T_{22})\hat{\mathbf{y}} + (T_{12} - T_{21})\hat{\mathbf{x}}\hat{\mathbf{y}}$. While the first term on the right is a scalar, and the next two are vectors, the last term appears to be a new type of axis represented by the unit vector $\hat{\mathbf{x}}\hat{\mathbf{y}}$. Indeed, it is in CA: The term $\hat{\mathbf{x}}\hat{\mathbf{y}}$ is a unit bivector, which is formed from the geometric product between the two unit vectors $\hat{\mathbf{x}}$ and $\hat{\mathbf{y}}$ (see Supplemental Material Section S2.2). In particular, $\hat{\mathbf{x}}\hat{\mathbf{y}}$ represents a unit area in the $\hat{\mathbf{x}}$ - $\hat{\mathbf{y}}$ plane. It has a clockwise circulation of vectors $\hat{\mathbf{x}}$ and $\hat{\mathbf{y}}$ around its perimeter (see **Figure 15**). Similarly, $\hat{\mathbf{y}}\hat{\mathbf{x}}$ represents a unit area with a counterclockwise circulation of vectors around its perimeter, such that $\hat{\mathbf{x}}\hat{\mathbf{y}} = -\hat{\mathbf{y}}\hat{\mathbf{x}}$, which is the condition for orthogonality between two vectors in CA. If one is wondering how to multiply two vectors, $\hat{\mathbf{x}}$ and $\hat{\mathbf{y}}$, in this fashion, one can, for example, define $\hat{\mathbf{x}} = (0.1; 1.0)$ and $\hat{\mathbf{y}} = (10; 0-1)$ —that is, as two 2×2 Pauli matrices. Then $\hat{\mathbf{x}}\hat{\mathbf{y}} = (0-1; 10) = -\hat{\mathbf{y}}\hat{\mathbf{x}}$. In addition, one finds that $\hat{\mathbf{x}}\hat{\mathbf{x}} = \hat{\mathbf{y}}\hat{\mathbf{y}} = (1\ 0\ ;\ 0\ 1) = I$, a unit matrix. Starting from a 2D (n=2) vector space spanned by $\hat{\mathbf{x}}$ and $\hat{\mathbf{y}}$, one is thus led to a $2^n = 4$ D CA space of I, $\hat{\mathbf{x}}$, $\hat{\mathbf{y}}$, and $\hat{\mathbf{x}}\hat{\mathbf{y}}$, composed of a scalar axis spanning the real number subspace, two vector axes spanning a vector subspace, and a bivector axis defining its own subspace. This can be generalized to any dimension (see Supplemental Material Section S2.2). In this manner, physical properties conventionally expressed as tensors can be rewritten as multivectors in CA. By doing so, Gopalan (11) recently showed that there are only 41 types of multivectors in arbitrary dimensions.

5.3. Dropping Axial and Chiral Traits in Generalizing to *n* Dimensions

To classify multivectors in general, however, the traits of axiality and chirality—and, as a consequence, the mirror operation, m_{\parallel} —in **Figure 14** need to be dropped. The idea of axial vectors is

Supplemental Material >

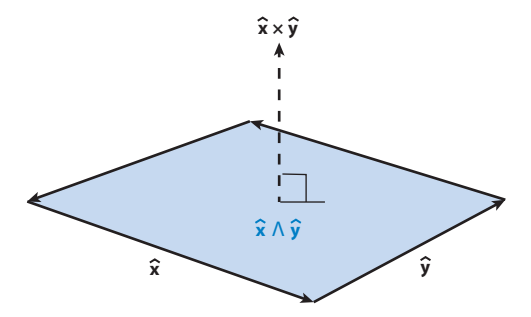


Figure 15

Schematic showing that the wedge product $\hat{\mathbf{x}} \wedge \hat{\mathbf{y}} = \hat{\mathbf{x}}\hat{\mathbf{y}}$ is a bivector whose magnitude is the unit area shown in blue with the counterclockwise circulation of vectors around its perimeter, while the cross product, $\hat{\mathbf{x}} \times \hat{\mathbf{y}} = \hat{\mathbf{z}}$, is a vector whose magnitude is the unit area and that points in the direction normal to the unit area. They are Hodge duals of each other, defined as $\hat{\mathbf{x}} \wedge \hat{\mathbf{y}} = \hat{\mathbf{x}}\hat{\mathbf{y}}\hat{\mathbf{z}}(\hat{\mathbf{x}} \times \hat{\mathbf{y}})$, where $\hat{\mathbf{x}}\hat{\mathbf{y}}\hat{\mathbf{z}}$ is a trivector in three dimensions.

not generalizable beyond three dimensions (with the curious exception of seven dimensions) (71). For example, in a 2D ambient space, the 2D loop in **Figure 14** has no normal at all, while in a 4D ambience, it has two normals. Thus, axial vectors have to be dropped in favor of bivectors. Chirality of an object in dimension n is tested conventionally by creating its mirror image with a mirror (a hyperplane) of dimension n-1 and looking for congruent overlap between the original image and mirror image; if they can be congruently overlapped, the n-dimensional (nD) object is achiral in nD space, and otherwise, the nD object is chiral in nD space. Now, referring to **Figure 16**, in

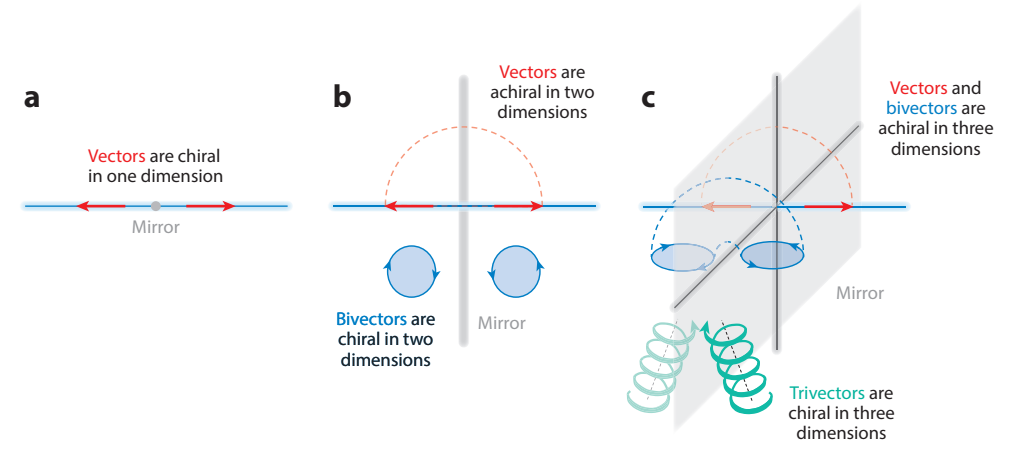


Figure 16

Schematic showing that the chirality of an object depends on the dimensionality of the ambient space it resides in. (a) A vector and its mirror image (red arrows) cannot be congruently overlapped in one dimension, and hence the vector is chiral. (b) However, a vector and its mirror image can be overlapped congruently in two dimensions, indicating that the vector is achiral. But a bivector and its mirror image, depicted by light blue circles with right-handed and left-handed circulations around their perimeters, cannot be congruently overlapped in two dimensions, indicating that bivectors are chiral in two dimensions. (c) Both a vector and a bivector are achiral in three dimensions, as indicated by light red and light blue broken lines denoting the suggested trajectory for overlapping the objects and their mirror images. However, a trivector, represented in light green by a helical structure, and its mirror image cannot be congruently overlapped in three dimensions, and hence it is chiral; it will no longer be chiral in four or more dimensions.

an nD space, only an nD object can be chiral. However, the same nD object will become achiral in a space of dimensionality n + 1 or higher. We thus conclude that the trait of chirality is also not unique to an object without reference to the dimensionality of its ambient space. Next, we describe wedge reversion, 1^{\dagger} , proposed recently by Gopalan (11), which resolves both these issues.

5.4. Wedge Reversion, 1[†], as a Missing Antisymmetry

Wedge reversion is not a new operation; it is simply called reverse, or reversion in CA (69, 70). What is new in the recent work by Gopalan (11) is that it is being formally given the status of an antisymmetry, 1^{\dagger} . To define 1^{\dagger} , we first need to define a wedge product between two vectors **A** and **B** as $\mathbf{A} \wedge \mathbf{B}$ (see **Supplemental Material Section S2.2** for a formal definition of wedge product). For example, if $\mathbf{A} = 5\hat{\mathbf{x}} + 2\hat{\mathbf{y}}$ and $\mathbf{B} = 2\hat{\mathbf{x}} - 3\hat{\mathbf{y}}$, then $\mathbf{A}\mathbf{B} = 4I - 19\hat{\mathbf{x}}\hat{\mathbf{y}}$, where we have made use of the orthonormality conditions (see Section 5.2 and **Supplemental Material Section S2.2**) that $\hat{\mathbf{x}}\hat{\mathbf{x}} = \hat{\mathbf{y}}\hat{\mathbf{y}} = I$ and $\hat{\mathbf{x}}\hat{\mathbf{y}} = -\hat{\mathbf{y}}\hat{\mathbf{x}}$. In this example, $\mathbf{A} \cdot \mathbf{B} = 4I$ (a scalar) and $\mathbf{A} \wedge \mathbf{B} = -19\hat{\mathbf{x}}\hat{\mathbf{y}}$ (a bivector). The product $\mathbf{A} \wedge \mathbf{B}$ (a bivector) is different from the conventional cross product, $\mathbf{A} \times \mathbf{B} = -19\hat{\mathbf{z}}$ (a vector); the former lives in the bivector subspace, while the latter lives in the vector subspace. Also, one should note that $\hat{\mathbf{x}}\hat{\mathbf{y}} = \hat{\mathbf{x}} \wedge \hat{\mathbf{y}}$, etc.

Geometrically speaking, the magnitude of $A \wedge B$ is the area of the parallelogram formed by vectors A and B; the two vectors define a sense of circulation around the edges of this area. This sense of circulation is reversed in $B \wedge A$. There is no reference to the dimensionality of the ambience of this object, only to the dimensionality of the object itself; hence, the wedge product is generalizable. Similarly, the wedge product between three linearly independent vectors, $A \wedge B \wedge C$, gives the 3D volume of the parallelepiped enclosed by the three vectors. To generalize, the wedge product between n linearly independent vectors gives the hypervolume enclosed by those vectors in n dimensions.

Wedge reversion, 1^{\dagger} , simply reverses the order of vectors in a wedge product, as depicted in **Figure 17**. In particular, consider the 3D Euclidean space spanned by the orthonormal basis vectors $\hat{\mathbf{x}}$, $\hat{\mathbf{y}}$, and $\hat{\mathbf{z}}$. Then, $1^{\dagger}(\hat{\mathbf{x}}) = \hat{\mathbf{x}}$, $1^{\dagger}(\hat{\mathbf{x}} \wedge \hat{\mathbf{y}}) = \hat{\mathbf{y}} \wedge \hat{\mathbf{x}} = -\hat{\mathbf{x}} \wedge \hat{\mathbf{y}}$, and $1^{\dagger}(\hat{\mathbf{x}} \wedge \hat{\mathbf{y}} \wedge \hat{\mathbf{z}}) = \hat{\mathbf{z}} \wedge \hat{\mathbf{y}} \wedge \hat{\mathbf{x}} = -\hat{\mathbf{x}} \wedge \hat{\mathbf{y}} \wedge \hat{\mathbf{z}}$. These relations follow from the orthonormality conditions given in **Supplemental Material Section S2.2**. Thus, wedge reversion, 1^{\dagger} , leaves the scalars and the vectors invariant but reverses the bivector, $\hat{\mathbf{x}} \wedge \hat{\mathbf{y}}$, and the trivector, $\hat{\mathbf{x}} \wedge \hat{\mathbf{y}} \wedge \hat{\mathbf{z}}$. Generally, 1^{\dagger} will reverse the sign of multivectors of grades 4g + 2 and 4g + 3 while leaving the multivectors of grades 4g and 4g + 1 invariant, where $g = 0, 1, 2, 3, \ldots$ is a whole number. That 1^{\dagger} reverses the sign of some multivectors while not reversing that of others led Gopalan (11) to use the term wedge reversion rather than wedge reversal.

A note of caution regarding the action of 1^{\dagger} and $\bar{1}$ axial vectors versus bivectors follows: the wedge reversion, 1^{\dagger} , will reverse a bivector, $\mathbf{A} \wedge \mathbf{B}$, but not the vector, $\mathbf{A} \times \mathbf{B}$, which is consistent with the discussion above that grade 1 multivectors are invariant under 1^{\dagger} and emphasizes that there is only one type of vector, not several. For the same reason, $\bar{1}$ will reverse $\mathbf{A} \times \mathbf{B}$ but leave $\mathbf{A} \wedge \mathbf{B}$ invariant similar word of caution exists between a trivector and a pseudoscalar in three dimensions: The action of 1^{\dagger} on a pseudoscalar, $(\mathbf{A} \times \mathbf{B}) \cdot \mathbf{C}$, is no different from its action on a conventional scalar, s; that is, they are both invariant under the action of 1^{\dagger} and $\bar{1}$.

5.5. Classification of Multivectors According to the Actions of $\bar{1}$, 1', and 1[†]

Using the traits of centric ($\bar{1}$ -even) versus acentric ($\bar{1}$ -odd) and circulant (1[†]-odd) versus acirculant (1[†]-even) blades, Gopalan (11) classifies multivectors as shown in **Figure 18**. (The term circulant avoids the term axial for reasons mentioned in Section 5.2.) As intuitive examples, the first four types of objects in **Figure 18** are centric-acirculant (scalar), acentric-acirculant (vector),

Supplemental Material >

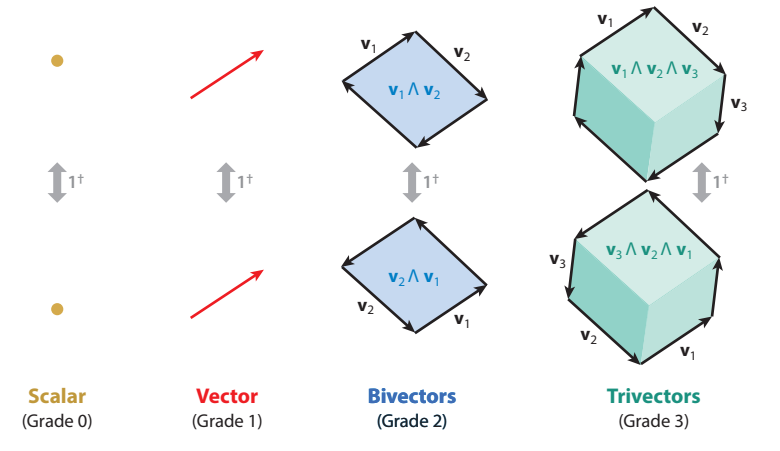


Figure 17

The action of wedge reversion, 1^{\dagger} , on multivectors of grades 0, 1, 2, and 3, where, specifically, $1^{\dagger}(s) = s$, $1^{\dagger}(\mathbf{v}) = \mathbf{v}$, and $1^{\dagger}(\mathbf{v}^{(1)} \wedge \mathbf{v}^{(2)} \wedge \mathbf{v}^{(3)} \dots \wedge \mathbf{v}^{(n-1)} \wedge \mathbf{v}^{(n)}) = \mathbf{v}^{(n)} \wedge \mathbf{v}^{(n-1)} \dots \wedge \mathbf{v}^{(3)} \wedge \mathbf{v}^{(2)} \wedge \mathbf{v}^{(1)}$, where *s* is a scalar, **v** is a vector, and $\mathbf{v}^{(i)}$ (*i* is the vector index, equal to 1, 2, 3, ..., *n*) are *n* linearly independent vectors. Bivectors and trivectors reverse under the action of 1^{\dagger} , while scalars and vectors do not. Unlike in **Figure 14**, no reference is made to axiality (cross products) or chirality (which requires one to consider the dimensionality of the ambient space the multivector resides in); these descriptions are dropped. Wedge reversion is well defined for an arbitrary-grade multivector residing in an arbitrary dimension of the ambient space.

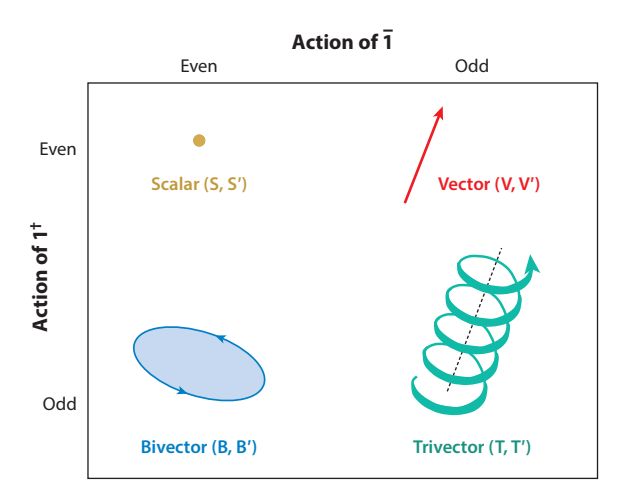


Figure 18

Eight types of multivectors in three dimensions. They are labeled S', V', B', and T' for time-even and S, V, B, and T for time-odd multivectors. The axial vector quantity, $\mathbf{r} \times \mathbf{T}$ from Figure 14, would instead be treated as a bivector quantity, $\mathbf{r} \wedge \mathbf{T}$, in the above classification. Similarly, the chiral quantity $(\mathbf{r} \times \mathbf{T}) \cdot \mathbf{n}$ from **Figure 14** would instead be treated as a trivector quantity, $\mathbf{r} \wedge \mathbf{T} \wedge \mathbf{n}$, in the above classification. In general, the classification proceeds as multivectors of grades 4g, 4g + 1, 4g + 2, and 4g + 3, where $g = 0, 1, 2, 3, \ldots$, respectively being either S', V', B', and T' for time-even and S, V, B, and T for time-odd multivectors (see **Table 1**). The case of g = 0 is depicted in the figure.

Action of Number Label 1′ 1† Type Grade Examples t^2 , $(\mathbf{r} \cdot \mathbf{P})$, $[(\mathbf{r} \times \mathbf{P}) \cdot \mathbf{n}]$ t-even centric-acirculant e e e 2 r, P, E 4g + 1t-even acentric-acirculant 3 $\overline{(\nabla \wedge \mathbf{P}), (\mathbf{r} \wedge \mathbf{P})}$ B't-even centric-circulant 4g + 2e e O 4 T'4g + 3 $(B') \wedge \mathbf{n}$; e.g., $\mathbf{r} \wedge \mathbf{P} \wedge \mathbf{n}$ e t-even acentric-circulant 5 S t-odd centric-acirculant 4gt, $(\mathbf{r} \cdot \mathbf{p})$, $[(\mathbf{r} \times \mathbf{J}) \cdot \mathbf{n}]$ o e $\overline{\mathbf{v}}$ 6 t-odd acentric-acirculant $\mathbf{v}, \mathbf{J}, \mathbf{p}, (\nabla \times \mathbf{S}), (\mathbf{E} \times \mathbf{H})$ O 4g + 17 В t-odd centric-circulant 4g + 2*H, *S, *B, $r \wedge J$ 8 Т 4g + 3 $(B \wedge n)$; e.g., $r \wedge J \wedge n$ t-odd acentric-circulant

Table 1 Antisymmetry-based classification of eight principal types of multivectors

Labels for eight multivector types (column 1) are introduced in column 2. Columns 3–5 present the action of three antisymmetries $(\bar{1}, 1', \text{ and } 1^{\dagger})$ on these multivectors as either even (e; invariant) or odd (o; sign reversal). Column 6 presents the type of multivector, and column 7 gives the grade of the multivector, where $g = 0, 1, 2, 3, \ldots$ is a whole number. Column 8 presents some examples of multivectors in three dimensions. Conventional polar vectors are presented in bold letters. Multivector types (column 2) are presented as nonbold, nonitalic capital letters. Bold letters are reserved for vectors, such as **P**, which is a time-even polarization vector measured in units of coulombs per square meter. The vectors **r** and **n** are two linearly independent vectors. Other definitions are as follows: **E** is electric field, **v** is velocity, **J** is current density, **p** is momentum, **H** is magnetic field, **B** is magnetic induction, **S** is spin, and t is time. Asterisks indicate, for example, ${}^*\mathbf{B} = \hat{\mathbf{x}}\hat{\mathbf{y}}\hat{\mathbf{z}}$ **B** in three dimensions, and similarly for others. For n dimensions, $\hat{\mathbf{x}}\hat{\mathbf{y}}\hat{\mathbf{z}}$ is replaced by the geometric product of the n basis vectors spanning those dimensions. The asterisk operation is the Hodge dual operation in Clifford algebra. A wedge product, for example, $\mathbf{B} \wedge \mathbf{n}$, is between a vector \mathbf{n} and any bivector of type B. Any cross product such as $\mathbf{r} \times \mathbf{P}$ is considered a vector that is odd under inversion, $\hat{\mathbf{I}}$, while ${}^*(\mathbf{r} \times \mathbf{P}) = \mathbf{r} \wedge \mathbf{P}$ is a bivector that is even under $\hat{\mathbf{I}}$.

centric-circulant (bivector), and acentric-circulant (trivector). Each one can be time-even or time-odd, leading to eight types of multivectors.

Table 1 lists the eight principal types of multivectors that are either invariant or reversed under the action of $\bar{1}$, 1', and 1[†]. Physical quantities and properties can be expressed as multivectors; hence, this classification is broadly applicable to classifying all properties. The table also lists some examples of such physical properties. If the action of these antisymmetries on a multivector can also be mixed (i.e., neither even nor odd), then there will be a total of 41 types of multivectors, as listed recently by Gopalan (11, table 1). The multivectors presented in **Table 1** here, however, are termed principal because all other multivector types arise from various sums of these principal multivectors. Since tensors can be expressed as multivectors, this classification suggests that there are eight principal and 41 overall types of tensors or tensor components that can be expressed as multivectors.

6. SUMMARY AND OUTLOOK

6.1. Why Are There So Few Antisymmetries?

It is remarkable that an abstract but simple idea such as an antisymmetry that switches between two states of a trait can have such practical applications in materials research and in physical sciences at large. Antisymmetry operations reviewed here, such as between forward and backward time or spins (time reversal, 1' or \mathcal{T} classically, and Θ Θ_S in quantum mechanics), positions between r and -r in space (inversion, $\bar{1}$, in the context of proper rotations), between forward and reverse motion of atoms in a distortion path (distortion reversal, 1*), and reversing the circulation of n linearly independent vectors that define a hypervolume in n dimensions (wedge reversion, 1[†]), can lead to powerful ways of describing the structure and symmetry of materials, physical quantities, and distortion paths and to a wide variety of very practical applications in crystallography, describing physical laws; polar and magnetic materials; quantum mechanics; general distortions

such as diffusion, vibrations, phase transitions, and polar and magnetic domain switching; finding MEPs; mapping energy surfaces; and the classification of multivectors.

Given the simplicity and usefulness of these antisymmetries, it is also equally surprising that since 1892, when the crystallographic groups were first listed, only a handful of the antisymmetries reviewed here have been used in materials research. We believe that there must be many more such useful antisymmetries that remain to be discovered. By the same token, the topic of permutation symmetry groups formed from more than two colors (19, 20, 72) (see **Figure 2***b* for example) could be more widely exploited in materials research, another area of opportunity for materials researchers.

6.2. Symmetry and Topology

An area of great current and growing interest is that of topological phenomena in materials research; many excellent reviews on the topic have been written (49, 73–75). We briefly note the relationship between symmetry and topology, which are two closely related concepts, and in particular the role of antisymmetries 1', $\bar{1}$, and 1^* in determining topological phenomena.

Symmetry operations, namely, rotations, rotoinversions, and translations, as well as antisymmetry operations, are distance preserving; that is, they preserve the norm (length) of a vector in the object on which they are operating. Thus, the internal angles and scaling are preserved under the action of symmetry operations, and the object is self-congruent before and after the operation is performed. In contrast, a topological operation allows for a continuous deformation of the object, as long as no cuts and stitches are made in the object. The object need not be self-congruent before and after the topological operation is performed.

The concept of symmetry plays a prominent role in topologically nontrivial states of matter. Here, symmetries of the material preserve the topological characteristics that result in distinct symmetry-protected topological phases. In other words, the Hamiltonian of a material that exhibits topological character cannot be adiabatically deformed to one that does not without breaking the protecting symmetry (73). One of the most common types of these phases studied comprises those protected by the antisymmetry of time reversal. More specifically, topological insulators with this property have become a popular topic of study in recent years (49, 73–75).

The protection of topological states in insulators through time-reversal symmetry (Θ_S) is a result of the Kramers degeneracy that arises for Bloch states in the band structure of the material (see Section 3.3; **Figure 8**). Kramers degeneracy ensures that a set of wavevectors (k-points) are deemed time-reversal invariant momenta (TRIMs), as applying the time-reversal operation Θ_S leaves each of them completely invariant to within a reciprocal lattice vector \mathbf{G} . In two dimensions, four unique TRIM points exist, while in three dimensions, there are eight. It can be shown that consideration of these TRIMs is enough to calculate the indices of the Z_2 (v_0 ; v_1 , v_2 , v_3) invariant, a quantity that characterizes the topological properties (48, 76, 77). A nonzero v_0 index indicates a strong topological insulator with surface states that are robust to disorder. Nonzero values of the other indices indicate weak topological characteristics where the same states vanish in the presence of local changes to the structure that break translational symmetry. In the presence of inversion symmetry, $\bar{1}$, the so-called Fu-Kane parity criteria (76) are widely used to easily characterize whether a given centrosymmetric material is a topological insulator.

Finally, we note a clean result connecting distortion-reversal antisymmetry, 1*, and the Berry phase (47), an important topological parameter in phenomena such as the Aharonov-Bohm effect (50) and the modern theory of polarization (78) in crystals. VanLeeuwen & Gopalan (10) showed that if a topological distortion path is distortion-reversal symmetry invariant—that is, if the path has explicit 1* symmetry—then the Berry phase will be identically zero. This result illustrates the power of an antisymmetry to obviate the need for further computation or measurements.

Distortion groups are currently not employed in the field of topology, but we believe that they could play an important role in uniquely tagging each topological distortion path and bringing the power of group theory to bear on the problems of classifying and discovering new topological phenomena.

DISCLOSURE STATEMENT

The authors are not aware of any affiliations, memberships, funding, or financial holdings that might be perceived as affecting the objectivity of this review.

ACKNOWLEDGMENTS

V.G. acknowledges wonderful discussions with Daniel B. Litvin, Brian VanLeeuwen, Chaoxing Liu, Hirofumi Akamatsu, Mantao Huang, Vincent S. Liu, Yin Shi, Long-Qing Chen, Craig J. Fennie, and Mikael C. Rechtsman. The concepts of distortion reversal and wedge reversion would not have come this far without these valuable interactions. V.G. thanks the late Robert E. Newnham for his gift of handcrafted wooden octahedra connected with ball-and-socket joints, which triggered the original rotation reversal symmetry idea. V.G., I.D., and H.P. acknowledge support in writing this article from the National Science Foundation (grant DMR-1807768) and the Center for Nanoscale Science at Penn State, a National Science Foundation Materials Research Science and Engineering Center (grant DMR-1420620).

LITERATURE CITED

- 1. Wigner EP. 1964. Symmetry and conservation laws. PNAS 51(5):956-65
- Newnham RE. 2005. Properties of Materials: Anisotropy, Symmetry, Structure. Oxford, UK: Oxford Univ. Press
- Trolier-McKinstry S, Newnham RE. 2017. Materials Engineering: Bonding, Structure, and Structure-Property Relationships. Cambridge, UK: Cambridge Univ. Press
- Fedorov ES. 1891. Симмтрія правильныхъ системъ фигурь. Zap. Imp. St. Petersburgskogo Mineral. Obshchestva 2(28):1–146
- 5. Schönflies AM. 1891. Kristallsysteme und Kristallstruktur. Leipzig, Ger.: B.G. Teubner
- Burckhardt JJ. 1967. Zur Geschichte der Entdeckung der 230 Raumgruppen. Arch. Hist. Exact Sci. 4:235–46
- Friedrich W, Knipping P, Laue M. 1913. Interferenzerscheinungen bei Röntgenstrahlen. Ann. Phys. 346(10):971–88
- Zamorzaev AM, Palistrant AF. 1980. Antisymmetry, its generalizations and geometrical applications. Z. Krist. Cryst. Struct. 151(3–4):231–48
- 9. Zamorzaev AM. 1988. Generalized antisymmetry. Comput. Math. Appl. 16(5-8):555-62
- 10. Van Leeuwen BK, Gopalan V. 2015. The antisymmetry of distortions. Nat. Commun. 6:8818
- Gopalan V. 2020. Forty-one types of physical quantities in arbitrary dimensions. Acta Crystallogr. A 76:318–27
- 12. Deleted in proof
- Hestenes D. 2015. Geometric calculus. In Space-Time Algebra, pp. 63–85. Cham, Switz.: Birkhäuser.
 2nd ed
- Aroyo MI, Kirov A, Capillas C, Perez-Mato JM, Wondratschek H. 2006. Bilbao Crystallographic Server. II. Representations of crystallographic point groups and space groups. Acta Crystallogr: A 62(2):115–28
- Aroyo MI, ed. 2016. International Tables for Crystallography, Vol. A: Space-Group Symmetry. Chester, UK: Int. Union Crystallogr.
- 16. Fennie CJ. 2008. Ferroelectrically induced weak ferromagnetism by design. Phys. Rev. Lett. 100:167203

- Ederer C, Fennie CJ. 2008. Electric-field switchable magnetization via the Dzyaloshinskii-Moriya interaction: FeTiO₃ versus BiFeO₃. 7. Phys. Condens. Matter 20(43):434219
- 18. Cotton FA. 1990. Chemical Applications of Group Theory. New York: Wiley-Interscience. 3rd ed.
- Lifshitz R. 1997. Theory of color symmetry for periodic and quasiperiodic crystals. Rev. Mod. Phys. 69(4):1181–218
- 20. Schwarzenberger RLE. 1984. Colour symmetry. Bull. Lond. Math. Soc. 16(3):209-40
- 21. Opechowski W. 1986. Crystallographic and Metacrystallographic Groups. Amsterdam: North-Holland
- Heesch H. 1930. Über die vierdimensionalen Gruppen des dreidimensionalen Raumes. Z. Krist. 73:325–
- Wills AS. 2017. A historical introduction to the symmetries of magnetic structures. Part 1. Early quantum theory, neutron powder diffraction and the coloured space groups. *Powder Diffr*. 32(2):148–55
- 24. Zamorzaev AM. 1953. Generalization of Fedorov groups. PhD Diss., Leningrad State Univ., USSR
- 25. Zamorzaev AM. 1957. Generalization of the Fedorov groups. Kristallografiya 2:15-20
- 26. Landau LD, Lifshitz EM. 1980. Statistical Physics. Amsterdam: Butterworth-Heinemann. 3rd ed.
- Gopalan V, Litvin DB. 2011. Rotation-reversal symmetries in crystals and handed structures. Nat. Mater. 10(5):376–81
- VanLeeuwen BK. 2015. The symmetry and antisymmetry of distortions. PhD Diss., Pa. State Univ., State College
- Munro JM, Akamatsu H, Padmanabhan H, Liu VS, Shi Y, et al. 2018. Discovering minimum energy pathways via distortion symmetry groups. Phys. Rev. B 98(8):085107
- Munro JM, Liu VS, Gopalan V, Dabo I. 2019. Implementation of distortion symmetry for the nudged elastic band method with DiSPy. NPT Comput. Mater. 5:52
- 31. Litvin DB. 2001. Magnetic space-group types. Acta Crystallogr. A 57(6):729-30
- 32. Litvin DB. 2013. Magnetic Group Tables. Chester, UK: Int. Union Crystallogr.
- VanLeeuwen BK, Gopalan V, Litvin DB. 2014. Double antisymmetry and the rotation-reversal space groups. Acta Crystallogr: A 70(1):24–38
- Huang M, Van Leeuwen BK, Litvin DB, Gopalan V. 2014. Crystallographic data of double antisymmetry space groups. Acta Crystallogr: A 70(4):373–81
- Padmanabhan H, Kingsland ML, Munro JM, Litvin DB, Gopalan V. 2017. Spatio-temporal symmetry point groups with time translations. Symmetry 9(9):187
- Liu VS, Van Leeuwen BK, Munro JM, Padmanabhan H, Dabo I, et al. 2018. Spatio-temporal symmetry crystallographic point groups with time translations and time inversion. Acta Crystallogr. A 74:399–402
- Landau LD, Pitaevskii LP, Lifshitz EM. 1984. Electrodynamics of Continuous Media. New York: Pergamon Press. 2nd ed.
- Shull CG, Smart JS. 1949. Detection of antiferromagnetism by neutron diffraction. Phys. Rev. 76(8):1256– 57
- Shull CG, Strauser WA, Wollan EO. 1951. Neutron diffraction by paramagnetic and antiferromagnetic substances. Phys. Rev. 83(2):333–45
- 40. Astrov DN. 1961. Magnetoelectric effect in chromium oxide. Sov. Phys. 7ETP 13(4):729-33
- Birss RR, Fletcher D. 1980. Space-time symmetry restrictions on transport coefficients. J. Magn. Magn. Mater. 15–18(2):915–16
- 42. Ashcroft NW, Mermin ND. 1976. Solid State Physics. Orlando, FL: Saunders Coll. Publ.
- Sakurai JJ, Napolitano J. 2017. Modern Quantum Mechanics. Cambridge, UK: Cambridge Univ. Press. 2nd ed.
- Watanabe H, Po HC, Vishwanath A. 2018. Structure and topology of band structures in the 1651 magnetic space groups. Sci. Adv. 4(8):eaat8685
- Wigner E. 1932. Über die Operation der Zeitumkehr in der Quantenmechanik. Nachr. Ges. Wiss. Gött. Math.-Phys. Kl. 1932:546–59
- Bigi II, Sanda AI. 2009. The strong CP problem. In CP Violation, pp. 314

 –32. Cambridge, UK: Cambridge
 Univ. Press
- 47. Kaxiras E, Joannopoulos JD. 2019. Quantum Theory of Materials. Cambridge, UK: Cambridge Univ. Press

- Moore JE, Balents L. 2007. Topological invariants of time-reversal-invariant band structures. Phys. Rev. B 75(12):121306
- 49. Ando Y. 2013. Topological insulator materials. J. Phys. Soc. Jpn. 82(10):102001
- 50. Peshkin M, Tonomura A. 1989. The Aharonov-Bohm Effect. Berlin: Springer-Verlag
- Bradley CJ, Cracknell AP. 1972. The Mathematical Theory of Symmetry in Solids. Oxford, UK: Oxford Univ. Press
- 52. Glazer AM. 1972. The classification of tilted octahedra in perovskites. Acta Crystallogr. B 28:3384–92
- 53. Ciullo PA. 1996. Silicate structures. In Industrial Minerals and Their Uses, pp. 1–16. Westwood, NJ: Noyes
- Boyle L, Khoo JY, Smith K. 2016. Symmetric satellite swarms and choreographic crystals. Phys. Rev. Lett. 116(1):15503
- 55. Pechukas P. 1981. Transition state theory. Annu. Rev. Phys. Chem. 32:159-77
- 56. Hratchian HP, Schlegel HB. 2005. Finding minima, transition states, and following reaction pathways on ab initio potential energy surfaces. In *Theory and Applications of Computational Chemistry*, the First Forty Years, ed. CE Dykstra, G Frenking, KS Kim, GE Scuseria, pp. 195–249. Amsterdam: Elsevier
- McKee ML, Page M. 1993. Computing Reaction Pathways on Molecular Potential Energy Surfaces. New York:
 VCH
- Henkelman G, Jónsson H. 2000. Improved tangent estimate in the nudged elastic band method for finding minimum energy paths and saddle points. J. Chem. Phys. 113(22):9978–85
- Henkelman G, Jóhannesson G, Jónsson H. 2002. Methods for finding saddle points and minimum energy paths. In *Theoretical Methods in Condensed Phase Chemistry*, ed. SD Schwartz, pp. 269–300. Dordrecht, Neth.: Springer
- Jonsson H, Mills G, Jacobsen K. 1998. Nudged elastic band method for finding minimum energy paths
 of transitions. In *Classical and Quantum Dynamics in Condensed Phase Simulations*, ed. BJ Berne, G Ciccotti,
 DF Coker, pp. 385–404. Singapore: World Sci.
- Ong SP, Richards WD, Jain A, Hautier G, Kocher M, et al. 2013. Python Materials Genomics (pymatgen): a robust, open-source python library for materials analysis. Comput. Mater. Sci. 68:314–19
- Nowadnick EA, Fennie CJ. 2016. Domains and ferroelectric switching pathways in Ca₃Ti₂O₇ from first principles. Phys. Rev. B 94(10):104105
- 63. Ye M, Vanderbilt D. 2016. Ferroelectricity in corundum derivatives. Phys. Rev. B 93(13):134303
- Heron JT, Bosse JL, He Q, Gao Y, Trassin M, et al. 2014. Deterministic switching of ferromagnetism at room temperature using an electric field. *Nature* 516(7531):370–73
- Baettig P, Ederer C, Spaldin NA. 2005. First principles study of the multiferroics BiFeO₃, Bi₂FeCrO₆, and BiCrO₃: structure, polarization, and magnetic ordering temperature. *Phys. Rev. B* 72(21):214105
- Lee D, Behera RK, Wu P, Xu H, Sinnott SB, et al. 2009. Mixed Bloch-Néel-Ising character of 180° ferroelectric domain walls. Phys. Rev. B 80(6):060102
- Hlinka J. 2014. Eight types of symmetrically distinct vectorlike physical quantities. Phys. Rev. Lett. 113(16):165502
- 68. Denker J. 2012. Introduction to Clifford Algebra. https://www.av8n.com/physics/clifford-intro.htm
- Snygg J. 2012. A New Approach to Differential Geometry Using Clifford's Geometric Algebra. New York: Springer
- 70. Doran C, Lasenby A. 2003. Geometric Algebra for Physicists. Cambridge, UK: Cambridge Univ. Press
- Massey WS. 1983. Cross products of vectors in higher dimensional Euclidean spaces. Am. Math. Mon. 90(10):697–701
- 72. Koptsik VA. 1988. Generalized symmetry in crystal physics. Comput. Math. Appl. 16(5-8):407-24
- Ando Y, Fu L. 2015. Topological crystalline insulators and topological superconductors: from concepts to materials. Annu. Rev. Condens. Matter Phys. 6:361–81
- 74. Yan B, Zhang SC. 2012. Topological materials. Rep. Prog. Phys. 75(9):96501
- Ren Y, Qiao Z, Niu Q. 2016. Topological phases in two-dimensional materials: a review. Rep. Prog. Phys. 79(6):66501
- 76. Fu L, Kane CL. 2007. Topological insulators with inversion symmetry. Phys. Rev. B 76(4):045302
- 77. Fu L, Kane CL, Mele EJ. 2007. Topological insulators in three dimensions. Phys. Rev. Lett. 98(10):106803
- Resta R, Vanderbilt D. 2007. Theory of polarization: a modern approach. In *Physics of Ferroelectrics*, ed. KM Rabe, CH Ahn, JM Triscone, pp. 31–68. Berlin: Springer



Volume 50, 2020

Contents

Data-Driven Discovery of Materials

Evolving the Materials Genome: How Machine Learning Is Fueling the Next Generation of Materials Discovery Changwon Suh, Clyde Fare, James A. Warren, and Edward O. Pyzer-Knapp
Machine Learning for Structural Materials Taylor D. Sparks, Steven K. Kauwe, Marcus E. Parry, Aria Mansouri Tehrani, and Jakoah Brgoch
Machine Learning in Materials Discovery: Confirmed Predictions and Their Underlying Approaches *James E. Saal, Anton O. Oliynyk, and Bryce Meredig
Opportunities and Challenges for Machine Learning in Materials Science Dane Morgan and Ryan Jacobs
Quantum Materials and Devices
Microwave Microscopy and Its Applications Zhaodong Chu, Lu Zheng, and Keji Lai
Angle-Resolved Photoemission Spectroscopy Study of Topological Quantum Materials Chaofan Zhang, Yiwei Li, Ding Pei, Zhongkai Liu, and Yulin Chen
Epitaxial Growth of Two-Dimensional Layered Transition Metal Dichalcogenides Tanushree H. Choudhury, Xiaotian Zhang, Zakaria Y. Al Balushi, Mikhail Chubarov, and Joan M. Redwing
Current Interest
Morphology-Related Functionality in Nanoarchitectured GaN Abhijit Chatterjee, Shashidhara Acharya, and S.M. Shivaprasad
Multiscale Patterning from Competing Interactions and Length Scales A.R. Bishop

Spontaneous Ordering of Oxide-Oxide Epitaxial Vertically Aligned Nanocomposite Thin Films Xing Sun, Judith L. MacManus-Driscoll, and Haiyan Wang
Antisymmetry: Fundamentals and Applications Hari Padmanabhan, Jason M. Munro, Ismaila Dabo, and Venkatraman Gopalan 255
Energy Conversion by Phase Transformation in the Small-Temperature-Difference Regime Ashley N. Bucsek, William Nunn, Bharat Jalan, and Richard D. James
Hybrid Thermoelectrics *fia Liang, Shujia Yin, and Chunlei Wan
Noble Metal Nanomaterials with Nontraditional Crystal Structures Chaitali Sow, Suchithra P, Gangaiah Mettela, and Giridhar U. Kulkarni
Muon Spectroscopy for Investigating Diffusion in Energy Storage Materials Innes McClelland, Beth Johnston, Peter J. Baker, Marco Amores, Edmund J. Cussen, and Serena A. Corr
High-Energy X-Ray Diffraction Microscopy in Materials Science Joel V. Bernier, Robert M. Suter, Anthony D. Rollett, and Jonathan D. Almer 395
Frontiers in the Simulation of Dislocations Nicolas Bertin, Ryan B. Sills, and Wei Cai
Grain Boundary Complexion Transitions Patrick R. Cantwell, Timofey Frolov, Timothy J. Rupert, Amanda R. Krause, Christopher J. Marvel, Gregory S. Rohrer, Jeffrey M. Rickman, and Martin P. Harmer
Recent Advances in Solid-State Nuclear Magnetic Resonance Techniques for Materials Research Po-Hsiu Chien, Kent J. Griffith, Haoyu Liu, Zhehong Gan, and Yan-Yan Hu
Self-Assembly of Block Copolymers with Tailored Functionality: From the Perspective of Intermolecular Interactions Rui-Yang Wang and Moon Jeong Park
Thermoelectric Properties of Semiconducting Polymers Kelly A. Peterson, Elayne M. Thomas, and Michael L. Chabinyc
Indexes
Cumulative Index of Contributing Authors, Volumes 46–50
Errata
An online log of corrections to <i>Annual Review of Materials Research</i> articles may be found at http://www.annualreviews.org/errata/matsci